Coastal Engineering 179 (2023) 104222

Contents lists available at ScienceDirect

Coastal Engineering

journal homepage: www.elsevier.com/locate/coastaleng

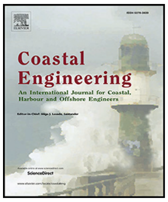

Large-scale experiments on tsunami inundation and overtopping forces at vertical sea walls

David J. McGovern [a,*], William Allsop [b], Tiziana Rossetto [c], Ian Chandler [d]

[a] School of The Built Environment and Architecture, London South Bank University, London, SE1 6LN, UK
[b] William Allsop Consulting Ltd, The White House Denchworth Road, Grove, Wantage, Oxon, England, OX12 0AR, UK
[c] Department of Civil, Environmental and Geomatic Engineering, University College London, WC1E 6BT, UK
[d] HR Wallingford, Howbery Park, Wallingford, Oxfordshire, OX10 8BA, UK

ARTICLE INFO

Keywords:
Experiments
Tsunami
Wall
Force
Overtopping
Bores

ABSTRACT

Tsunami are very long gravity waves that may cause significant damage to coastal sea walls. The majority of relevant design codes and research papers that describe methods for predicting tsunami loads on coastal walls consider the scenario of transitory force from a bore-led wave. This does not relate to tsunami that do not form bore waves. Bore fronts generally cause short term spikes in force, which may have little effect on the vulnerability of massive structures. Post disaster accounts suggest that most coastal walls show damage that implies failure modes that occur over moderate to long durations. Therefore it is likely that the bore front assumption gives an overly conservative prediction of maximum force, and may not capture the full timescale of tsunami loading. This paper uses a pneumatic tsunami generation facility to determine the force loading on two vertical coastal sea walls during tsunami inundation. Two sea-wall models, 0.15 and 0.25 m high, with crown widths of 0.1 m (7.5 and 12.5 m at a nominal prototype scale of 1:50) are tested. It is shown that bore fronts only occur for short period waves over the bathymetry tested. Bore fronts cause a very short period spike in force, which is followed by a transitory force approximated by the hydrostatic pressure equation. The loading of tsunami length waves of periods ≥40 s (280 s prototype at 1:50 scale), which do not break is not greater than 1.2 times the hydrostatic force. Overtopping volume is positively correlated to the time duration of positive upstream head over the crest, rather than its maximum value. Overtopping causes a small increase in the horizontal load due to the addition of a drag and momentum load. The magnitude and time of these effects are small and short-lived in comparison to the hydrostatic load. The results compare well with available equations based on hydrostatic force and the engineer may apply a desired multiplying coefficient of a factor of at least 1.2 to account for any added pressure and momentum, and the factor of safety intended.

1. Introduction

Tsunami are very long shallow-water progressive gravity waves that can be generated by sea floor displacement due to mega-thrust fault earthquakes or landslides. Tsunami inundate the coastal built environment, some of which may be protected by sea walls. The 2004 Indian Ocean Tsunami (IOT) and 2011 Tohoku Earthquake and Tsunami (TET) cumulatively killed approximately 300,000 people and caused billions of dollars in economic and infrastructure losses (Kajitani et al., 2011 and Nandasena et al., 2012). TET caused significant damage to coastal defences and in some cases caused their total failure (see field surveys by EEFIT, 2011, EEFIT, 2013, Mori and Takahashi, 2012, Chock et al., 2013 and Fraser et al., 2013). A number of different failure modes of seawalls are identified by these surveys including:

- foundation sliding and/or overturning due to hydrostatic or buoyancy forces on the sea and shoreward side of walls
- scour of the rear toe foundation during overtopping
- high velocity flows through wall member joints undermining foundations and/or exposing internal fill material

In some cases the overtopping flow generated a lift force on the top concrete capping of walls, which then failed due to a lack of strength in the vertical direction, exposing the aggregate infill. Raby et al. (2015) give a detailed review of the TET interaction with and damage pathways of coastal defences on the Japanese coast. The majority of the failure modes surveyed are the result of the long period inundation of the tsunami, not instantaneous impact forces due to bore inundation, of which the majority of research has focussed on to date.

---

* Corresponding author.
E-mail address: mcgoverd@lsbu.ac.uk (D.J. McGovern).

https://doi.org/10.1016/j.coastaleng.2022.104222
Received 5 May 2022; Received in revised form 14 September 2022; Accepted 25 September 2022

Nomenclature

List of Symbols

a^+	Positive wave amplitude [m]
a^-	Negative wave amplitude [m]
b	Width of structural element [m]
C_d	Drag coefficient
C	Celerity [m s^{-1}]
C_{exp}	Celerity [m s^{-1}]
d	Water depth [m]
E_p	Potential energy of the wave [J m^{-1}]
F_h	Hydrostatic force calculated from hydrostatic theory [N]
F_x	Horizontal force calculated from integration of pressure readings [N]
$F_{x,predicted}$	Horizontal force calculated from predictive equations [N]
$F_{x,b}$	Horizontal body force [N]
f	Wave frequency [Hz]
g	Acceleration due to gravity [m s^{-2}]
H	Wave height [m]
H_i	Defined incident wave height [m]
H_1	Upstream head height ($h_{max} - h_{wall}$) [m]
h	Water height [m]
h_a	Water height at front face of the wall [m]
h_b	Water height at rear face of the wall [m]
h_e	Height of bore including the still water depth [m]
h_j	Height of propagating bore [m]
h_{wall}	Height of the wall [m]
h_{max}	Maximum water height at the wall [m]
H_D	Design wave height [m]
I	Tsunami importance factor
k	Wave number
L_b	Wetted bathymetry length [m]
p_{av}	Average wave pressure $[pa]$
P	Total pressure $[pa]$
p_{max}	Maximum pressure on front face of wall $[pa]$
Q	Flow discharge per unit width [m^2 s^{-1}]
q_{av}	Mean overtopping discharge rate per unit width [m^2 s^{-1}]
q_{peak}	Peak overtopping discharge rate per unit width [m^2 s^{-1}]
R_c	Wall crest freeboard [m]
R	Wave runup [m]
T	Wave period $[s]$
t_o	Overtopping time $[s]$
u	Flow velocity [m s^{-1}]
u_{max}	Maximum flow velocity [m s^{-1}]
V_{tot}	Maximum overtopping volume per unit width [m^2]
v_j	Bore velocity [m s^{-1}]
X	Coordinates in the horizontal direction [m]
Z	Coordinates in the vertical direction [m]
z	Still water depth at the wall [m]
α	A constant, or slope angle [degrees]
δ_0	Height of clapotis [m]
η	Free surface elevation [m]
η_{max}	Maximum free surface elevation [m]
λ	Wavelength [m]
ρ	Density of water [kg m^{-3}]

In response to the sea defence failures caused by the TET, the Japanese authorities have implemented a two-level tsunami hazard classification based on return period and inundation depth at a particular location (Shibayama et al., 2013). The classifications are broad and require localised interpretation. All coastal defences must defend against a 'level 1' event (return period 50–60 to 150–160 years typically 7–10 m inundation height) and remain structurally intact throughout a 'level 2' event (return period a few hundred to a few thousand years $\geq$ 10 m, encompassing up to 20–30 m inundation height). Defences are expected to be overtopped during a 'level 2' event and, therefore, must be designed to retain structural integrity during overtopping. Historically, overtopping is considered a failure mode for a sea defence, with wave overtopping volume commonly used to determine the performance of a sea defence (e.g., Goda, 2010 and Goda, 1995). To date there is little understanding or data on tsunami inundation and overtopping forces and volumes, which would be useful for assessment of sea wall performance against tsunamis.

Much of the knowledge of the physical process of tsunami inundation and the forces imparted on the walls during inundation is inferred from post-event surveys such as those by EEFIT (2011, 2013), Chock et al. (2013). Laboratory simulation is also used to generate data sets from which empirical equations are developed and numerical models may be validated. A number of laboratory simulations assume bore-led tsunami, and use the dam-break generation method to study this (detailed in Section 2.2). This method, however, may be less well suited to reproduce the time-velocity-flow depth scaling of the succeeding tsunami wave that the bore front precedes. Tsunami may also inundate without a significant bore front. Field (ASCE, 2022) and experimental (McGovern et al., 2019) measurements have shown that maximum tsunami overland velocities are often found at approximately 2/3 of the maximum tsunami height h_i, and at approximately 1/3 of the tsunami period T. While there are several design methods that include tsunami onshore effects such as Goda et al. (2014), FEMA (2000) and ASCE (2022), for the specific case of sea defences, engineers still have access to relatively limited and disparate data and guidance on tsunami forces. Of particular use would be the forces induced from overtopping and inundation of long period waves.

1.1. Aims

This paper examines the inundation and overtopping of Froude-scaled tsunami-length trough and crest-led waves on two vertical onshore sea-walls of different heights. The aims are to:

1. measure the maximum and time-dependent tsunami forces at the wall.
2. measure the tsunami overtopping volume and rates at the wall.
3. explore the parameters affecting the recorded force and overtopping volumes.

The paper utilises a novel pneumatic tsunami generation system to reproduce tsunami-length waves at Froude scale, and is amongst the first to address their impact and overtopping with sea walls. The results will provide a clearer understanding of the loading profiles and overtopping rates and volumes on a sea wall under tsunami inundation. The quantification of these forces may provide validation data for numerical studies and aid future design methods and standards.

The paper is structured as follows. Available codes and guidance for tsunami inundation of coastal defences are reviewed. Gaps in the data on tsunami inundation of coastal defences are then identified. Next, the laboratory set-up and methodology of a set of experiments is described. The results are then presented starting with a description of typical inundation characteristics, including impulsive and pulsating impacts, and overtopping processes. The data are then compared with appropriate equations and the sensitivity of force to selected parameters are discussed. Finally discussions, conclusions and recommendations for future research are given.

2. Design codes and equations for wave and tsunami forces at coastal defences

Most sea walls are designed primarily to resist actions of wind waves and swell (Goda, 1974 and Thomas and Hall, 1992). Wind wave loading on coastal structures can be divided into 'pulsating' (non-breaking), or 'impulsive' (from breaking and broken waves). Extensive research into both these types of inundation (for example, Cuomo et al., 2003, Cuomo et al., 2010a and Cuomo et al., 2010b) have led to detailed design and prediction methodologies being made available to the engineer, such as the British Standard (BSI, 2000), the Shore Protection Manual (US Army Corps of Engineers, 1984), Coastal Engineering Manual (US Army Corps of Engineers, 2006) and EurOtop, (Van der Meer et al., 2018). Goda (2010), provides a detailed review of the available methodologies for wind wave inundation and overtopping forces on sea defences of various types.

Methods to calculate pulsating loads on sea walls are well established (Goda, 1995). Hiroi (1920) proposes Eq. (1) to predict the average wave pressure:

$$p_{av} = 1.5\rho g H_D \tag{1}$$

Where p_{av} is the average wave pressure [pa], ρ is the density of water [kg m^{-3}], g is acceleration due to gravity [ms^{-2}] and H_D is the design wave height [m]. The design wave height is generally assumed to be measured at the wall. Pressure is assumed to act from whichever is the smallest between either the base of the vertical part of the structure to $1.25H_D$ or the height of the wall. This equation is based on field recordings of breaking wave impact pressures during the construction of the Otaru Port Breakwater in 1912–1917.

Sainflou (1928) presents Eq. (2) for the total pressure P at vertical walls due to non-breaking standing waves.

$$\begin{aligned} P &= (p_2 + \rho g h)(H_D + \delta_0) \\ p_2 &= \frac{\rho g H_D}{cosh kh} \\ \delta_0 &= \frac{\pi H_D^2}{\lambda} coth\, kh \end{aligned} \tag{2}$$

where P is the total pressure, λ is the wavelength, $k = 2\pi/\lambda$ wave number, δ_0 is the height of the clapotis at the wall. The Shore Protection Manual (US Army Corps of Engineers, 1984) suggests the Sainflou method (Sainflou, 1928) performs best for long waves of lower steepness but may overestimate forces for steep nonbreaking waves. The Sainflou method uses trochoidal theory to estimate δ_0 from a given H_D and is limited to water depths $d > 2H_D$.

2.1. Pulsating tsunami loads — no leading bore

Tsunami loading on a sea wall may consist of two phases depending on the characteristics of the inundating wave. If bore-led the initial inundation at the wall may be impulsive and short-lived. This is followed by a second phase of a quasi-steady pulsating load. In the absence of a leading bore, the inundation may only be characterised by a pulsating load. Recently, the impulsive bore impact phase has received increased attention (discussed in Section 2.2), yet few guidelines for the design and assessment of coastal defences to tsunami existed before the TET, for example, CCH (2000), FEMA (2008), Goda et al. (2002). The Japanese Ports and Harbours Bureau (Goda et al., 2002) technical standard allows tsunami pressures on a breakwater to be estimated from Eq. (3).

$$p_{max} = 2.2\rho g a^+ \tag{3}$$

Where p_{max} is the maximum pressure on the front face of the structure at the still water level and a^+ is the positive amplitude above mean water level of the incident tsunami wave [m]. The location in which a^+ is defined is dependent on a number of factors. For an unbroken wave a^+ coincides with the highest water level at the wall. For a bore led tsunami a^+ is taken as the height directly behind the bore front. Eq. (3) is derived by Tanimoto et al. (1983) from experimental bore impact data in a 163 m long flume. The coefficient 2.2 appears to be the result of a linear fit to the experimental data. The maximum inundation height of the tsunami is given as $3a^+$.

Post 2011, a revised technical standard (Goda et al., 2014) suggests the tsunami load is numerically modelled for each particular site. Tsunami propagation over local topographies can be numerically modelled using computational fluid dynamic packages such as SWAN (Holthuijsen et al., 1993), COULWAVE (Lynett et al., 2008), and NHWAVE (Ma et al., 2012). The explicit modelling of flow-structure interaction is often substituted with roughness coefficients based on land use to avoid increasing complexity, computational cost and error. If a suitable numerical model is unavailable, other undefined methods are to be used. Presumably this would be empirical predictor equations based on laboratory and/or field data.

2.2. Impulsive tsunami bore loads

Relatively more attention has been afforded to tsunami bore inundations. Extensive experimental and numerical research has produced a variety of empirical equations to predict tsunami bore forces on vertical walls including Cross (1967), Ramsden and Raichlen (1990), Ramsden (1996), Yeh (2006), Robertson et al. (2013), Kihara et al. (2015), and for the case of coastal structures Shafiei et al. (2016), Tomiczek et al. (2016) (for bore led long waves) and Foster et al. (2017) (for unbroken long waves). This research has filtered into design codes such as the Federal Emergency Management Agency code (FEMA, 2000), where equation for the tsunami bore hydrodynamic and hydrostatic forces are given. The hydrostatic force on a structure is given in Eq. (4)a, while the resultant hydrostatic force on a structure considering the water level at the rear is given by Eq. (4)b.

$$F_{hs} = \frac{1}{2}\rho g b h^2 \tag{4a}$$

$$F_{hs} = \frac{1}{2}\rho g b (h_a^2 - h_b^2) \tag{4b}$$

where b is the width of the element normal to the flow [m], h is the maximum water height above the base of the structure and h_a and h_b are the time-coincident heights of water on the front and rear of the structure respectively [m].

The ASCE/SEI 7-22 (ASCE, 2022) codes provide hydrodynamic and drag force expressions for buildings which account for the difference in upstream and downstream water levels. They assume a decoupling of the impulsive, hydrodynamic drag and hydrostatic forces and neglect the effect of the structure on the flow. Eq. (5) to calculate F_x, where $b < 3h_{max}$, in which h_{max} is the maximum inundation height at the structure. The value u is the presumed maximum tsunami velocity [ms^{-1}] or momentum flux (hu^2), taken to occur at $\frac{2}{3}$ inundation height. Eq. (6) is expressed on vertical structural components magnified by an additional tsunami importance factor I.

$$F_x = \frac{1}{2}\rho I C_d b (hu^2) \tag{5}$$

The bore impingement process generally lasts for seconds (as seen in, Robertson et al., 2013 and Kihara et al., 2015), after which quasi-steady inundation may continue for several minutes as the later parts of the tsunami overflows the structure. For bore-led tsunami, the horizontal force time history observed on a sea wall can consist of three phases (e.g. Kihara et al., 2015:

1. Impulsive phase (from the bore impact)
2. Intermediate phase (transition between impulsive bore impact and quasi-static forces due to the 'flipped' – that is, collapsing of the vertically deflected – water mass effect from the initial bore inundation. Here both hydrostatic and hydrodynamic forces contribute)
3. Quasi-static phase (otherwise known as the pulsating phase, where the force is essentially hydrostatic)

This three phase time history is observed experimentally by Nouri et al. (2010), Palermo et al. (2013), Kihara et al. (2015) and numerically by Takabatake and Kihara (2014).

Kihara et al. (2015) examine the impulsive, intermediate and quasi-static phases of tsunami loading on a wall in the laboratory. It is shown that the impulsive phase can be further divided into two distinct short-lived pressure processes related to the impact of the bore with the wall containing significant entrapped air impact phase and the later water impact phase. Kihara et al. (2015) provide prediction equations based on the time scale of the impact phase. For the quasi-static phase, Palermo et al. (2009, 2013), Takabatake and Kihara (2014), Kihara et al. (2015), Foster et al. (2017) (for the case of blocking ratios < 1, where the blocking ratio is the width of the structure divided by the width of the channel in which it is sited), show the distribution of pressure at the wall or structure to be approximately hydrostatic. Therefore, F_h may be given as Eq. (6), as also permitted in ASCE (2022).

$$F_h = \rho g b \int_0^h (h - z) dz = \frac{1}{2} \rho g h^2 b \tag{6}$$

where h is the total height of water at the wall including z, which is the still water depth at the wall [m]. The quasi-static forces and quasi-steady flow velocities are temporally dominant features of the inundation process and appear to have been the primary cause of coastal defence failures during the TET event (see Section 1). Additionally, large concrete piled and gravity sea walls may not be very sensitive to very high but very short-lived pressures, Goda (2010).

2.3. Summary of current practice

The NILIM (2013) disaster scenario manual provides guidance on tsunami effects on coastal structures and design recommendations. This includes toe armouring for scour prevention and interlocking of segments to prevent their damage from uplift pressures. These design features are being implemented in post-TET sea wall construction in Japan, Raby et al. (2015). The ASCE/SEI 7-22 chapter 'Tsunami Loads and Effects' (ASCE, 2022), does not provide explicit guidance on the prediction of tsunami loading at coastal defences, or provide design guidance for these structures. Though as described above in Section 2.2, guidance is given for force calculations on buildings. There is brief mention of tsunami barriers in section 6.13.2 therein, which includes reference to the ability of any barrier (wall) to remain structurally intact during an overtopping event.

As it stands, the engineer is presented with a disparate set of guidance, much of which is not directly intended for tsunami inundation and overtopping of sea-walls. Those which are specific to tsunami, are commonly focussed on the bore-led portion of the tsunami. Yet as observed by McGovern et al. (2018), Foster et al. (2017) in their laboratory testing, when the full time-series of an incoming long tsunami wave is considered, the impinging wave is seldom characterised by a leading bore. When a bore is present, which is usually dependent on shallower nearshore topographies or may develop after some distance of overland flow, it only lasts for the initial seconds of wave, and this phenomena alone cannot account for the failure modes observed in the field.

In summary, the design engineer has relatively little guidance, and typically little experience of tsunami induced loads on a sea wall, leaving them few options other than the methods developed for wind waves and tsunami bore inundations. Improved knowledge of the characteristics of tsunami inundation and overtopping of a sea wall will allow improvements to the design of walls, aid numerical modelling and risk assessment by facilitating the prediction of the force on a defence as a function of the incident tsunami parameters.

3. Methodology

This paper presents experimental results from an extensive test programme designed to achieve the aims set out in Section 1.1. To generate tsunami-length waves at appropriate scale, this study uses the second generation of the Pneumatic Long Wave Generator (otherwise known as the Tsunami Simulator) method originally described in Rossetto et al. (2011). This iteration of the Tsunami Simulator (TS) allows the generation of Froude-scaled crest and trough-led tsunami waves in a 100 m long flume. The TS is a 4 m long 3.5 m high and 1.8 m wide machined steel box with a chamfered opening 0.4 m by 1.8 m at the base (total volume 21.6 m^3). Two vacuum pumps pump air out of the TS via pipes at the top allowing the internal air pressure to be varied by changing the angle of a butterfly valve in a third pipe. This varies the net pressure and hence the internal TS water head. This causes the spatial and time-dependent free-surface elevation $\eta(X,t)$; where X is the horizontal coordinate and t is time. Further details on the TS is given in McGovern et al. (2018), who conduct a validation of the method, its capability of producing Froude scaled prototype tsunami waveforms such as the 'Mercator' IOT waveform and an investigation of tsunami runup in the same flume in a test programme that preceded the experiments presented herein. They also discuss its advantages over other long wave generation systems namely its ability to produce Froude scaled large amplitude, long period tsunami waves. The development of the TS is described more completely in Chandler et al. (2021).

A coordinate system, defined in Fig. 1 shows the TS is installed at $X = 0$ m; the far end of the 100 m long 1.8 m wide flume at HR Wallingford, U.K. The generated waves propagate down the flume over a constant depth region to the toe of the bathymetry located at $X = 65.6$ m. A 1:20 sloping bathymetry extends until $X = 84.93$ m and to a vertical height of 1 m. A vertical wall is installed with its toe positioned at $X = 84.93$ m. In all tests, the still water level is at the wall toe, meaning the crest freeboard height $R_c = h_{wall}$. A schematic of the flume is given in Fig. 1.

The free surface elevation ($\eta(t)$) is recorded at various positions along the flume in the offshore (constant depth region $X = 0.85, 7, 12, 17, 22, 27$ and 47 m, Fig. 1) and nearshore (above the sloping bathymetry $X = 65.6, 70.6, 75.6, 80.6, 83.6, 85.6, 86.6, 87.6$ and 88.9 m) regions of the flume using 16 resistance-type wave gauges (accuracy $>$ 0.0005 m, manufactured by HR Wallingford). The sampling rate is 100 Hz. These gauges are calibrated regularly and before each set of wave conditions (Appendix A).

An extensive suite of elevated (hereon referred to as crest-led) and trough-led waves with periods $T \approx 6$ to 240 s (model scale) are simulated (full parameters are given in Appendix A Table A.1), including 10 waveforms (prefixed TL or CL for trough and crest-led respectively) that are repeated two or more times (Table 1). For trough-led waves, T is calculated from the difference between time at the start of the trough t_{start} and the end of the crest t_{end} (Fig. 2a). Times t_{start} and t_{end} are respectively defined at the times of the first and second down-crossings of $\eta(X,t)$ across the value corresponding to 1% of the maximum positive amplitude a^+. The maximum negative $\eta(X,t)$ defines the negative amplitude a^-. For elevated waves t_{start} and t_{end} are defined as the times when $\eta(X,t)$ first up-crosses and then first down-crosses the value corresponding to 1% of a^+ respectively (Fig. 2b). Celerity

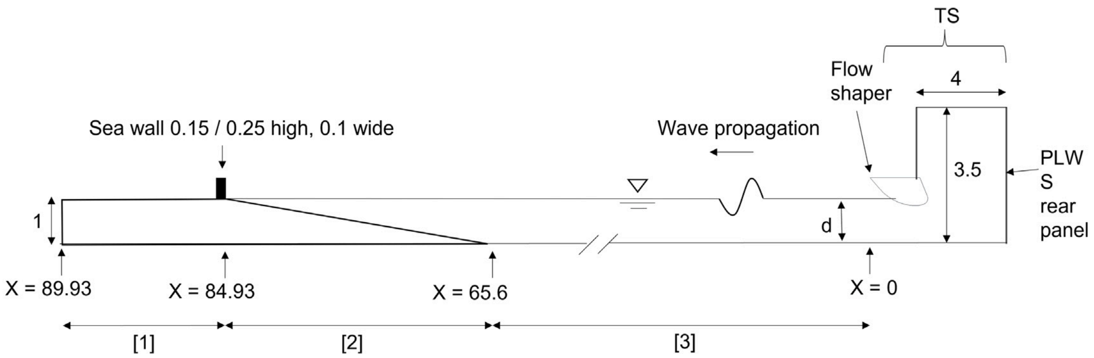

Fig. 1. Schematic of flume with the 2nd generation of the TS identifying the onshore [1], nearshore [2] and offshore [3] regions. Not to scale, all distances in metres.

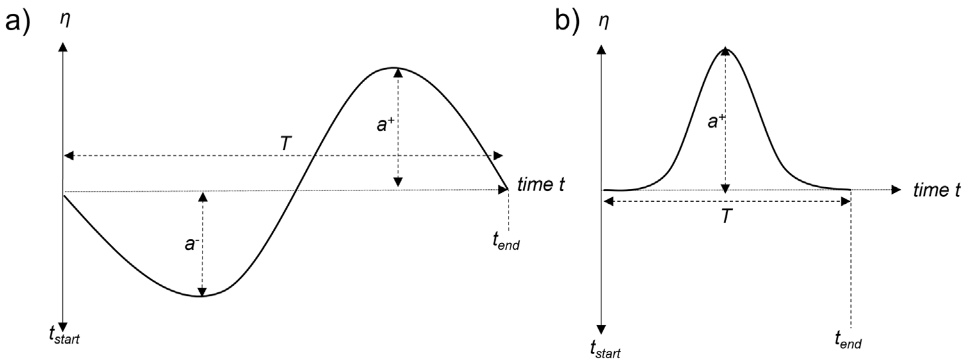

Fig. 2. Schematic of the definitions of (a) trough-led and (b), crest-led wave characteristics including period T, positive and negative amplitudes a^+ and a^- respectively, and t_{start} and t_{end}.

Table 1

Characteristics of the wave conditions that are repeated two or more times defined at $X = 65.6$ m where 'TL' and 'CL' denote trough and crest-led waves respectively. the standard deviation σ between the repeated waves is also given. The full range of wave conditions tested is summarised in Appendix A.

Trough/Crest-led Wave type	T [s]	a^+ [m]	a^- [m]	C_{exp} [m/s]	E_p [m]	λ [m]	d [m]	No. of repeats
TL20	22.64	0.05	−0.04	2.54	278.39	57.19	1.03	3
σ	1.03	0.00002	0.001	0.5	54.18	9.35	0.0003	
TL50	53.17	0.08	0.05	2.67	1057.41	134.35	1.03	4
σ	4.02	0.001	0.001	0.39	563.66	41.95	0.001	
TL80	77.81	0.08	−0.06	2.91	2180.77	231.34	0.92	3
σ	0.17	0.0002	0.001	0.35	195.36	37.81	0.0003	
TL95	93.28	0.064	−0.053	2.98	2003.51	208.2	0.92	2
σ	3.29	0.0005	0.0012	0.70	460.70	58.11	0.0003	
TL160	163.44	0.039	−0.037	2.37	1241.84	388.53	0.993	2
σ	3.42	0.001	0.001	0.959	497.07	91.58	0.001	
TL200	210.10	0.039	−0.039	2.17	1266.54	456.74	0.99	1
TL240	236.54	0.036	−0.037	2.40	2333.81	569.17	0.99	3
σ	1.16	0.0001	0.0006	0.89	1378.92	174.25	0.0003	
CL30	30.54	0.09	–	2.76	1152.64	83.85	0.95	3
σ	1.49	0.003	–	0.19	68.07	9.77	0.05	
CL40	40.50	0.094	–	3.16	2202.62	127.33	0.97	4
σ	1.70	0.01	–	0.48	605.71	13.31	0.04	
CL80	75.10	0.068	–	3.31	2378.84	249.71	0.97	4
σ	1.49	0.003	–	0.94	446.12	65.5	0.04	
CL200	194.94	0.055	–	3.18	3208.09	621.49	0.95	5
σ	16.79	0.002	–	0.84	866.99	170.63	0.05	

$C_{\exp}$, is calculated from the temporal correlation of the beginning of the waveform between the last offshore wave gauge ($X = 47.0$ m) and the bathymetry toe wave gauge ($X = 65.6$ m). The wavelength λ is defined as the product of celerity and period.

The waves are defined at $X = 65.6$ m from the Tsunami Simulator (TS, Fig. 1). This position is directly above the bathymetry toe. This position is chosen as it represents a location where reflections from the slope are manifest almost instantaneously on the waveform, and it constitutes a definitive change in slope that is easier to define rigorously in a prototype. Due to the very long wavelengths of the waves produced, their recording at any given point in the flume may be a composite of the incident and reflected components, with the main

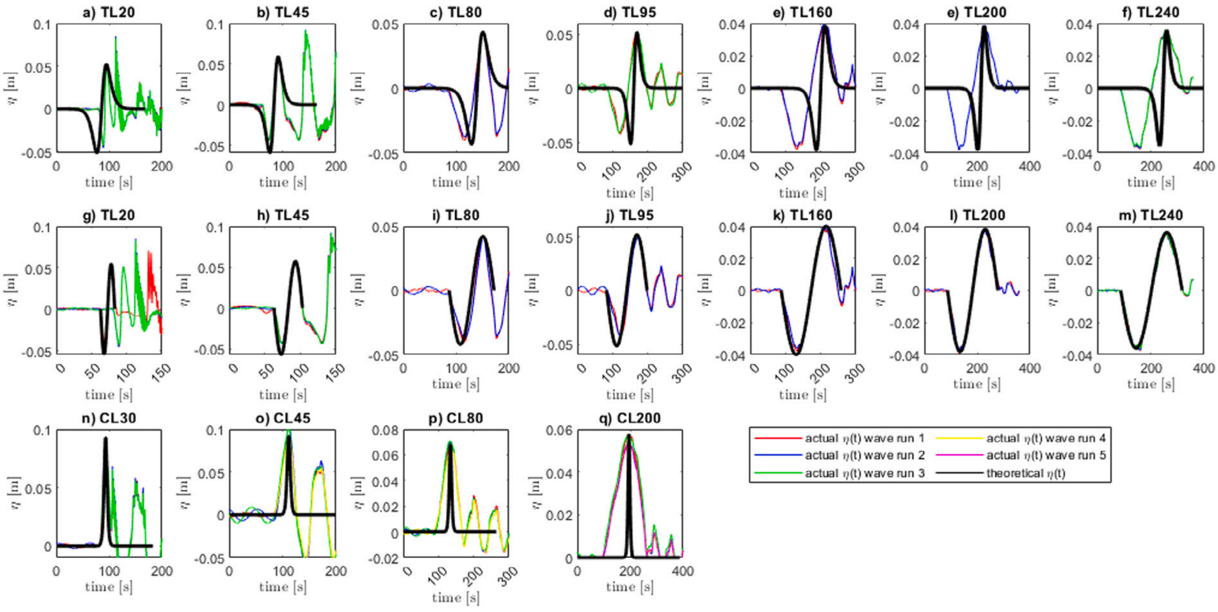

Fig. 3. The recorded time-series η for runs of the trough-led (TL) 20 s, 50 s, 80 s, 95 s, 160 s, 240 s, and crest-led (CL) 30 s, 40 s, 80 s and 200 s waves, along with the mathematically described $\eta(t)$ signal. The trough-led waves are compared with the theoretical N-wave shape given by Eq. (8) (Fig. 3a–g), the sine function $\eta(t) = a^{+}\sin(2\pi f t)$ (Fig. 3h–n) and the crest-led waves with the solitary wave Eq. (7) (Fig. 3o–r).

source of the reflection being the sloping bathymetry. The choice of the bathymetry toe as the point for defining the waves is discussed in detail in McGovern et al. (2018), who also show that the TS effectively absorbs reflections from the slope. Appendix A Fig. A.1, shows the propagation of a TL80 s wave.

The recorded (wave gauge at $X = 65.6$ m)and theoretical $\eta(t)$ for each change in T in the repeated wave set are presented in Fig. 3. The waves differ from the mathematical description of solitary (Eq. (7), Fig. 3a–g) and N-waves (Eq. (8), Fig. 3o–r). For trough-led waves, the calibration most closely follows a sine function (where $\eta(t) = a^{+}\sin(2\pi f t)$, Fig. 3h–n). The calibration for the crest-led waves uses the solitary wave solution for the C30 wave ($T = 30.5$ s, Fig. 3o) as the target, which fits the measured wave well. To achieve larger crest-led wave periods in these experiments, the wave shape was elongated to the desired period while retaining the largest amplitude possible given the finite volume capacity of the TS. This lead to smaller amplitudes for increasing wave periods and a wave shape that departed from the theoretical solitary wave profile but was more consistent with that of a real tsunami profile (for example, Figure I1 in McGovern et al., 2018).

$$\eta(X,0) = \frac{H}{d}\mathrm{sech}^2(K_s(X - X_1)) \tag{7}$$

$$\eta(X,0) = \alpha\frac{H}{d}(X - X_2)\mathrm{sech}^2(K_s(X - X_1)) \tag{8}$$

Two sea-wall models, 0.15 and 0.25 m high (7.5 and 12.5 m at a nominal prototype scale of 1:50) are used. The horizontal body force $F_{x,b}$ (positive landward) is recorded using a Kistler 9327C piezoelectric 3-axis load cell with a sensitivity of +/- 1 mN. The responsive wall segment of width $b = 0.1$ m is cantilevered off the load cell as shown in Figs. 4 and 5. There exists a two-millimetre gap between the responding segment and adjacent surfaces (floor and sides) are sealed with flexible latex sheet. The calibration method is discussed in Appendix B, and showed no evidence of friction from contact between surfaces. The sampling rate is 100 Hz.

The resolved force F_x (horizontal, positive landward) is calculated from the integration of pressure $p(z)$ readings (see Appendix B) from an array of 12 Trafag 160 mbar pressure transducers (Figs. 4 and 5). These are located at the following heights z [m] above the base of the wall (with the transducer number as depicted on Fig. 4 in parenthesis). For $h_{wall} = 0.25$ m; 0.0215 m (1), 0.0385 m (2), 0.0565 m (3), 0.0742 m (4), 0.0945 m (5), 0.1115 m (6), 0.1245 m (7), 0.1465 m (8), 0.1645 m (9), 0.1815 m (10), 0.1984 m (11) and 0.2215 m (12). For $h_{wall} = 0.15$ m there are ten transducers. These are located at $z = 0.018$ m (position (1), Fig. 4), 0.029 m (2), 0.04 m (3), 0.051 m (4), 0.064 m (5), 0.073 m (6), 0.084 m (7), 0.095 m (8), 0.108 m (9), 0.117 m (11). The sampling rate is 100 Hz. This is increased to 1000 Hz for selected tests where there is wave breaking to capture impulsive effects (such as in Fig. 9). The calibration method is discussed in Appendix B.

Three methods are used to record the time-series of water free surface elevation at the wall: (1) two pressure transducers are located at the corner interface between the front face of the wall and the flume side, positioned downward-facing to record the water pressure next to the base of the wall. These are separated by approximately 0.1 m from each other. (2) two wave gauges, each one close to each transducer but not close enough to cause interference between instruments. And 3), high-speed video imagery of the front face through the observation window. F_h is then estimated using Eq. (6) with $h = h_{max}$ (the maximum height of water recorded at the wall).

The overtopping volume per unit width of the wall is collected by a 0.26 m by 0.36 m container placed behind the wall and fed by a 0.1 m width collecting chute.

3.1. Scale considerations

The set-up of the experiment, is identical to that described in McGovern et al. (2018) experiments on tsunami runup, with the exception of the presence of the wall. Considerations of the scale effects are discussed in detail in Section 2.5 of McGovern et al. (2018). These are briefly examined here. There are 3 non-dimensional force ratios that may influence the physics of the wave propagation and inundation; the Froude number, Reynolds Number and Weber Number. The Froude number $Fr = \frac{U}{\sqrt{gd}}$ describes the ratio of the inertial forces with gravitational restoring forces, and for free surface flows is usually required to be in similitude between the model and the prototype. This is due to the dominance of gravity over other restoring forces such as fluid viscosity μ, who's importance is described by the Reynolds Number ratio $Re = \frac{Ud}{\mu}$ and the surface tension described by the Weber Number ratio $We = \frac{\rho U^2 l}{\sigma_s}$, where l is a characteristic length and σ_s is the surface tension. From Table 1, the minimum and maximum Re values (using C

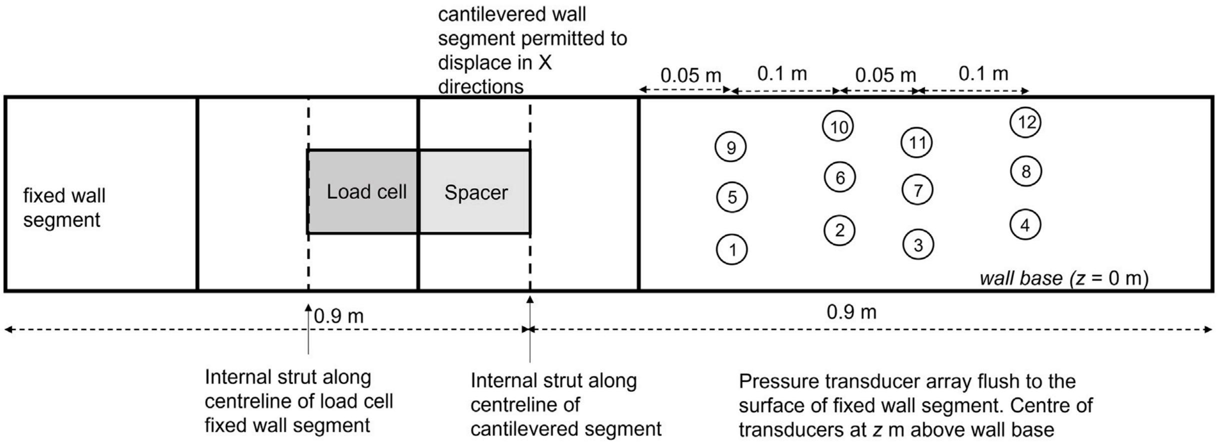

Fig. 4. Schematic of the front face of the wall, applicable to both the h_{wall} = 0.15 and h_{wall} = 0.25 m high wall. Not to scale.

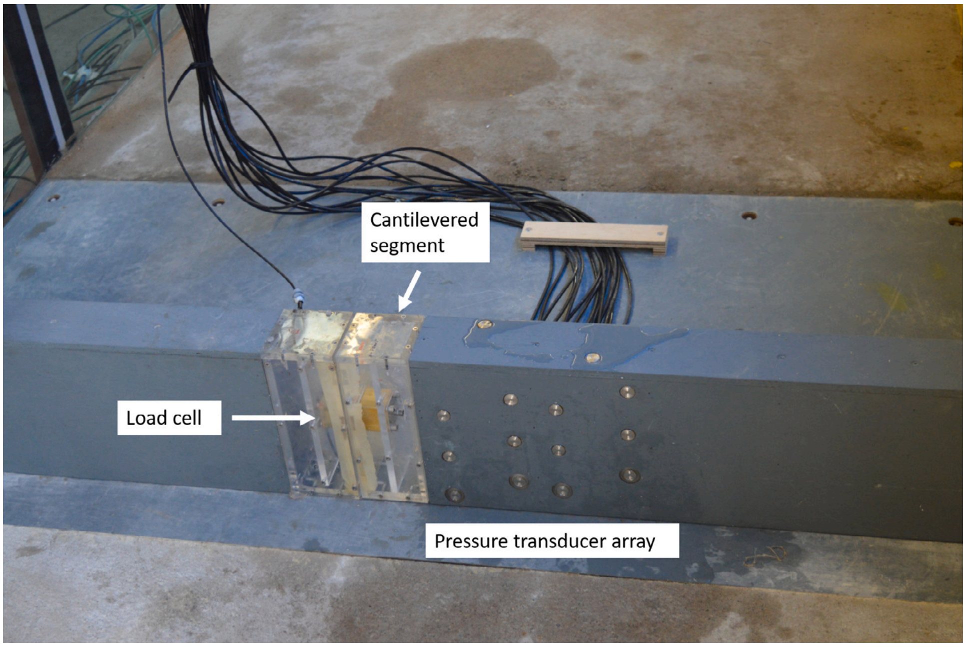

Fig. 5. Image of the h_{wall} = 0.25 m showing the load cell and pressure transducer array.

and d as the characteristic velocity and length) are 1.6 and 2.5 × 10^6 respectively, meaning that the fluid flow is in the fully turbulent regime in both model and prototype (Hughes, 1995). There are inevitably differences in the nature of the boundary layer around the walls, which may in some cases be laminar in the model as opposed to generally turbulent in the prototype. However it is argued that the boundary layer processes such as separation and vortex formation do not have significant influence on hydrostatic loading and overtopping processes modelled here. The We numbers are 2.9 and 4.4 × 10^4 respectively, which is well below the threshold for surface tension effects discussed by Peakall and Warburton (1996) of $We < 160$ below which surface tension effects become important. The scale effects of the experimental setup are further discussed in McGovern et al. (2018).

4. Results

The maximum force as a function of wave period is discussed first. Then the presence of impulsive impacts at short wave periods is analysed. The overtopping of the walls is characterised. Finally the results are compared with the most appropriate predictive equations.

4.1. Maximum force as a function of wave period

The maximum values of force F_x recorded at each wall are now discussed and compared against the expected component defined by hydrostatic theory. The comparison is made by normalising F_x with the theoretical hydrostatic estimation from using the recorded height of water at the wall, F_h. This is intended to identify whether the loading is hydrostatically dominated, and whether there are impulsive components.

The great majority of the dimensionless forces F_x/F_h plotted in Fig. 6 as a function of T are close to unity and F_x does not exceed an upper envelope of $1.2F_h$. This unity in theoretical and recorded hydrostatic force is observed in all non-breaking waves, regardless of period, suggesting there is minimal dynamic contribution to the load at the wall save some added momentum from the wave. At $T <$ 40 s a large number of breaking wave inundations occurred (un-filled data symbols on Fig. 6), where F_x/F_h approaches $25F_h$. There is no discernible difference between broken trough-led and crest-led waves. The observations show that for waves which do not break, the impact is of the pulsating type and the force imparted on the wall is well described by hydrostatic theory, with an upper envelope of $1.2F_h$. This

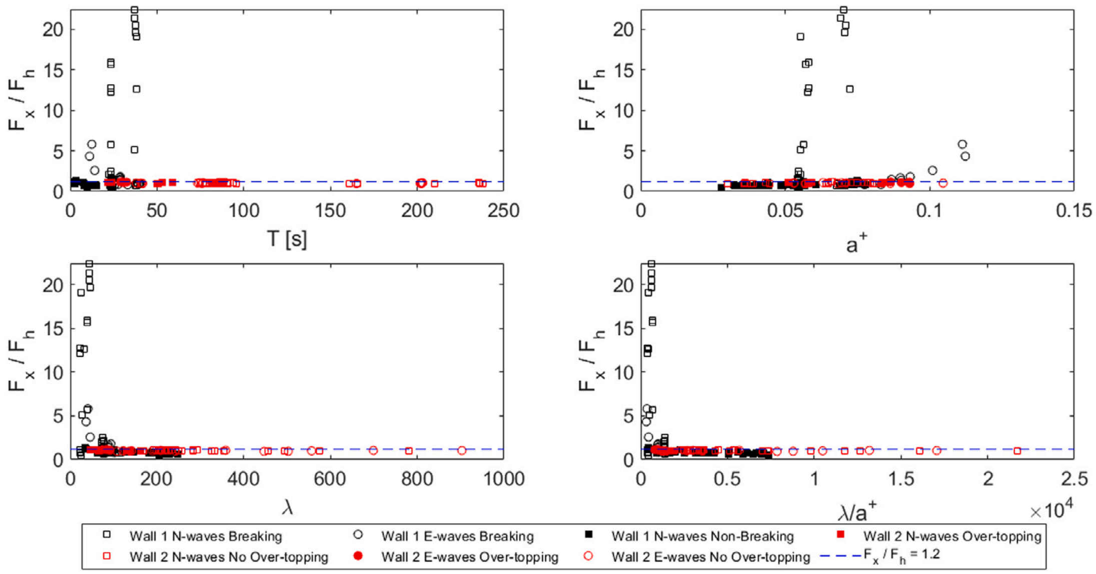

Fig. 6. F_x versus F_h for all waves tested.

is because these waves as generated by the tsunami simulator do not shoal enough over the beach slope to break, which is related to the wave steepness.

The inundation process is relatively slow and maximum water level h_{max} at the wall occurs with the arrival of the top of the wave crest. An analogy may be drawn with that of a standing wave inundation, where a linear depth-dependent pressure distribution occurs below the water level at the wall. F_x is therefore strongly related to h_{max}. However, Fig. 6 also indicates that for shorter waves there may be significant impulsive components that lead to rather large forces being recorded. This is discussed in Section 4.2.

4.2. Impulsive tsunami impact loads — breaker inundations

The waves described in the previous Section 4 range from T = 20–240 s. These scale at 1:50 to prototype periods of 140 s to 28 mins. The TET $T \approx 22$ mins and the IOT ≈ 14 mins which scale at 1:50 to ≈ 155 s and 120 s model respectively (see Appendix A.1 in McGovern et al., 2019). Therefore, modelled waves that are significantly below $\approx$ 100 s at 1:50 scale may not be representative of earthquake generated tsunami at prototype.

Notwithstanding, a significant portion of breaking waves in the shorter period region identified in Fig. 6 (T < 40 s), impart values of F_x that are up to an order of magnitude greater than F_h. To investigate the effect of broken wave impacts on the walls, a series of additional waves were generated of periods of approximately 20 s or less. These were specifically intended to break onto, or near the wall. This section will discuss this in more detail by comparing the time series loading profile of the measured force from the integration of pressures along the front face of the wall F_x, the theoretical hydrostatic force F_h and the body force measured by the load cell, $F_{x,b}$ for a typical impulsive inundation.

The majority of research on tsunami inundation with walls and structures considers the tsunami-bore phenomena (Section 2.2). Turbulent bores form when the wave starts to break before contact with the wall. These may generate impulsive forces much greater than F_h, (e.g., Nouri et al., 2010 and Kihara et al., 2015). In the described experimental set-up here, waves with $T \geq 40$ s did not break.

Fig. 7 shows recorded F_x (integration of pressure readings), $F_{x,b}$ (load cell response) and calculated F_h (from time-series water level at the wall) as a function of t for the inundation of a single run of a trough-led ≈ 20 s. While the non-dimensional force is given in Fig. 6, the dimensioned force is given to facilitate a focus on the physical characteristics of this single wave impact. This inundation time-series profile is typical of a short wave (defined here as T < 40 s), which break on, or very close to (within 0.3 m of), the wall. Several large impulsive peaks are observed in F_x that have total durations of ≤0.01 s. The first, at $t \approx 0$ s is just under 100 N and caused by the initial rebound off the flume floor of the wave front that has broken very close to the wall (approximately shown in Fig. 8a). The 2nd larger peak is >400 N at $t \approx 0.02$ s and related to the main impact of the wave front where the plunging breaker has entrapped the air 'tube' that then slams against the wall caused by the compression of entrained air (Fig. 8b). This is not captured by the load cell in $F_{x,b}$ likely due to the mechanical response frequency of the cantilever system that suspends the responding wall segment onto the load cell being significantly lower than that required to capture such high frequency events. It is also the case that F_x may overestimate the force due to the non-linear pressure distribution that occurs across the front face of the wall during the initial stages of inundation from a broken wave front as pictured in Fig. 8. The time series for all 12 wall transducers (with sampling rate set to 1000 Hz) shows large non-linearity in $p(z)$ (Fig. 9, with each sub-figure showing the vertical column of three transducers each as related to Figs. 4 and 5). F_x appears to be greater or equal to F_h in the impulsive phase but converges to F_h by $t \approx 2$ s. The overtopping is brief, (ending ≈ 2 s after the initial inundation), after which the loading quickly becomes quasi-static.

Between $t \approx 0.3$–2 s, F_x is higher than $F_{x,b}$. This can be attributed to both over estimation of F_x due to residual non-linearities (Fig. 8d suggests that air entrainment may remains significant at 1.88 s) and some reduction of $F_{x,b}$ due to overtopped water trapped in the developing, short-lived nappe on the landward side. This applies a negative value of $F_{x,b}$ in the seaward direction that reduces the resultant body force vector on the structure.

The collapse of the upwardly directed wave front occurs at $t \approx 0.4$ s. For inundations of turbulent bores this coincides with the reflection or transition phase and can exhibit forces higher than the impulsive force at the start of the inundation. There is some debate in the literature as to the exact mechanism(s) of this. Cross (1967) attributes it to the collapse of the reflected front back into the up-welling jet. Ramsden and Raichlen (1990) suggest vertical accelerations due to the upward reflection delay the maximum force occurrence. Bredmose et al. (2009.) suggest it is due to the pressure generated from the deceleration of the collapsing reflection. Kihara et al. (2015) suggest a combination of collapsing and incident forces. In the experiments reported here the collapse of the reflection is present in all waves of $T \leq 40$ s.

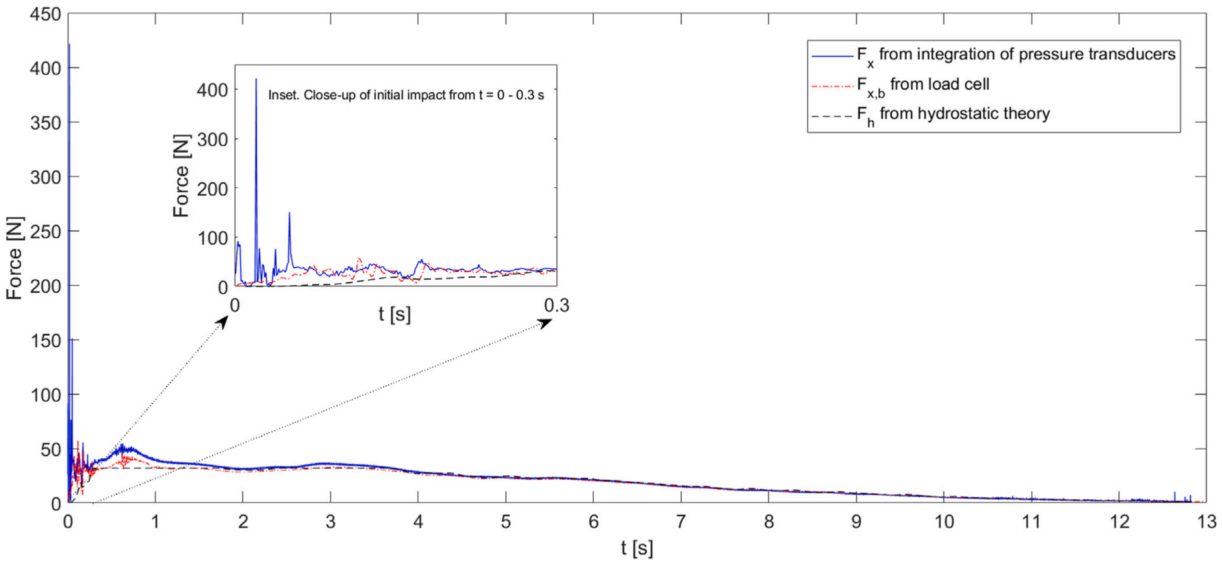

Fig. 7. F_x, $F_{x,b}$ and F_h as a function of t during the inundation of a TL20 s wave. Inset; close-up of region depicting initial impact from t = 0–0.3 s.

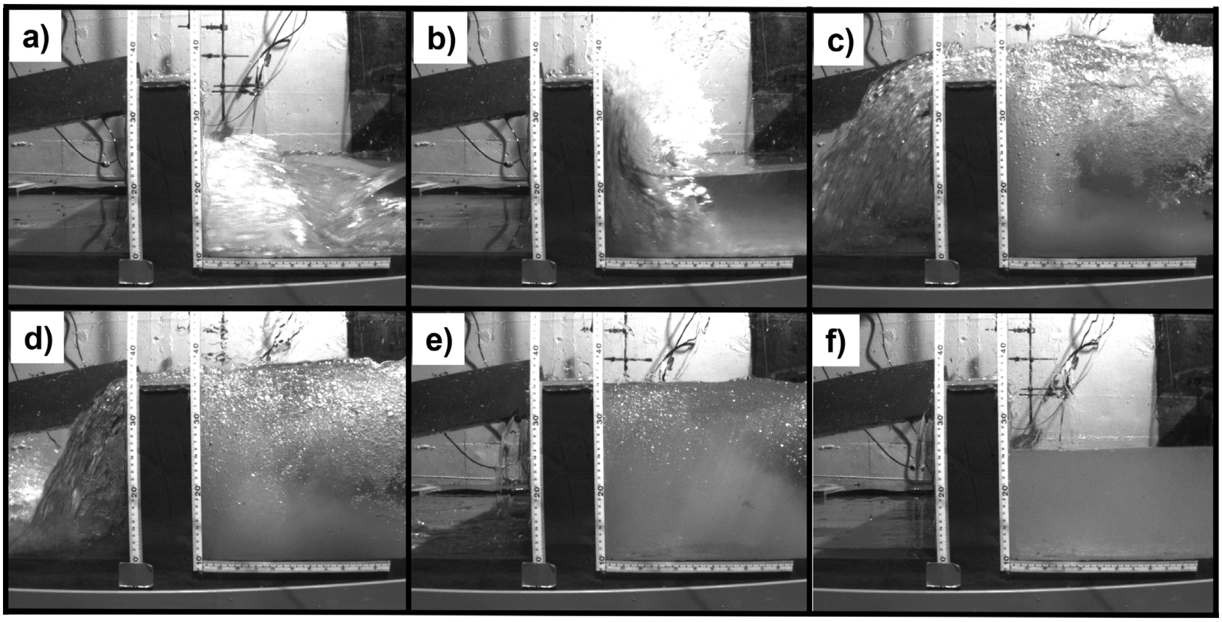

Fig. 8. Images of the initial inundation at 0 s, 0.17 s, 0.67 s (8a, 8b and 8c) and 0.88 s, 1.88 s and 7 s (8d, 8e and 8f).

4.3. Impulsive tsunami impact loads — bore inundations

The description of the wave inundation in the previous section is typical of a series of short waves that break close to the wall (within 0.3 m). In an additional selection of cases, a series of 8 $T \approx 23.5$ s trough-led waves were generated on the h_{wall} = 0.25 m wall. These waves are generated so as to break further seaward from the wall (>1 m), to encourage the inundation of a more developed turbulent bore, which might be more relevant to prototype broken tsunami wave inundations. The crests of these asymmetrical trough-led waves were shortened to encourage breaking at a position greater than 1 m seaward of the wall.

Time series F_x, $F_{x,b}$ and F_h for the inundation of one of these T = 23.5 s trough-led wave on the h_{wall} = 0.25 m wall are shown on Fig. 10. Fig. C.3 in Appendix C shows all eight waves recorded.

High-speed video images of the inundation that generates the force time history on Fig. 10 are extracted in Figs. 11a–d. As the broken wave front inundates the wall, the water is initially deflected vertically upward (Fig. 11a), resulting in the maximum value of F_h being recorded (Fig. 10, point [a]). F_x and $F_{x,b}$ record an ≈ 60% lower force suggesting that the initial impact of the wave front is characterised by a relatively high air content. This results in lower pressure and force readings compared to the theoretical hydrostatic force as calculated from the height of the free-surface. Eventually the deflected wave front collapses back onto the incoming wave (Fig. 11b), and this corresponds to the lowest value of F_h (Fig. 10, point [b]). At this point there is a large vortex between the incoming and reflected flow. F_x and $F_{x,b}$ are now approximately $\frac{2}{3}$ greater than F_h. This suggests the incoming wave has added impulsive pressure effects (F_x). The maximum values of F_x and $F_{x,b}$, (Fig. 10, point [c]), are observed when the inundation is most turbulent (Fig. 11c). Here, turbulent mixing is dominant and there is significant trapped air. Eventually, the loading becomes dominated by the hydrostatic component, as F_x and $F_{x,b}$ converge with F_h, indicating dynamic loading is no longer significant (Fig. 11d, which relates to

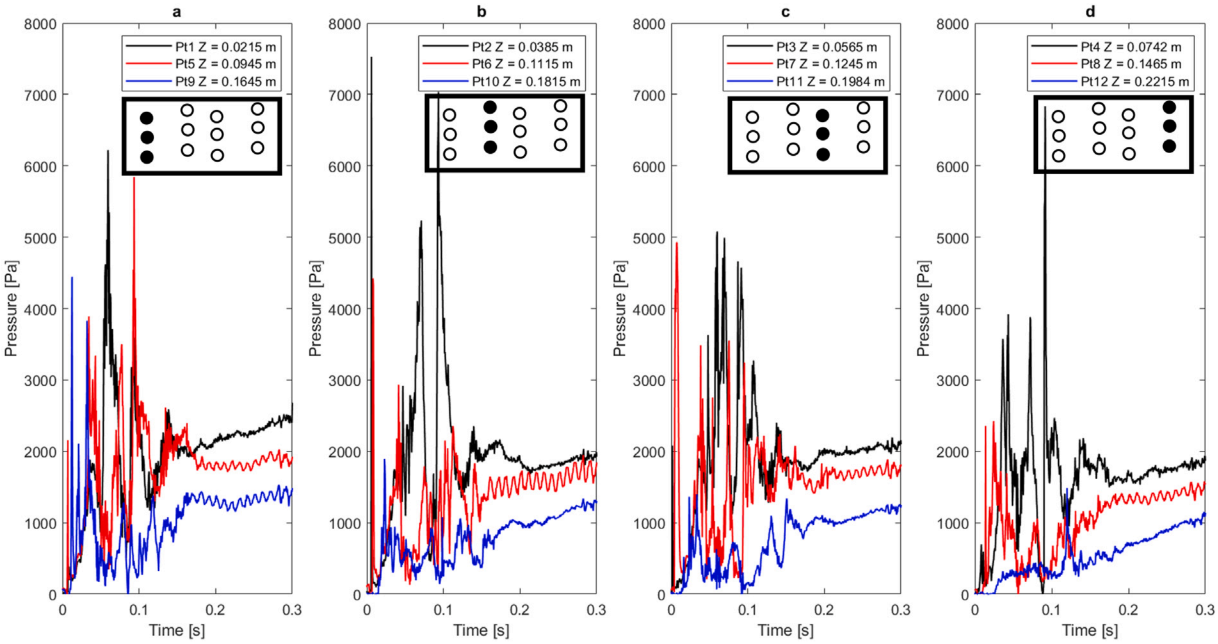

Fig. 9. a–d, p(t) for each transducer (sampling at 1000 Hz) at the wall face for the first 0.3 s of the inundation showing large non-linearity in the recorded pressures as a function of height. These are subdivided into the four vertical columns of three transducers relating to the positions shown in Figs. 4 and 5. The inset schematic below the legend in each subfigure indicates the column of pressure transducers on front face of the wall the subfigure is presenting. Z [m] relates to the absolute position of each transducer above the bed for the h_{wall} = 0.25 m starting with the lowest as described in Section 2.2.

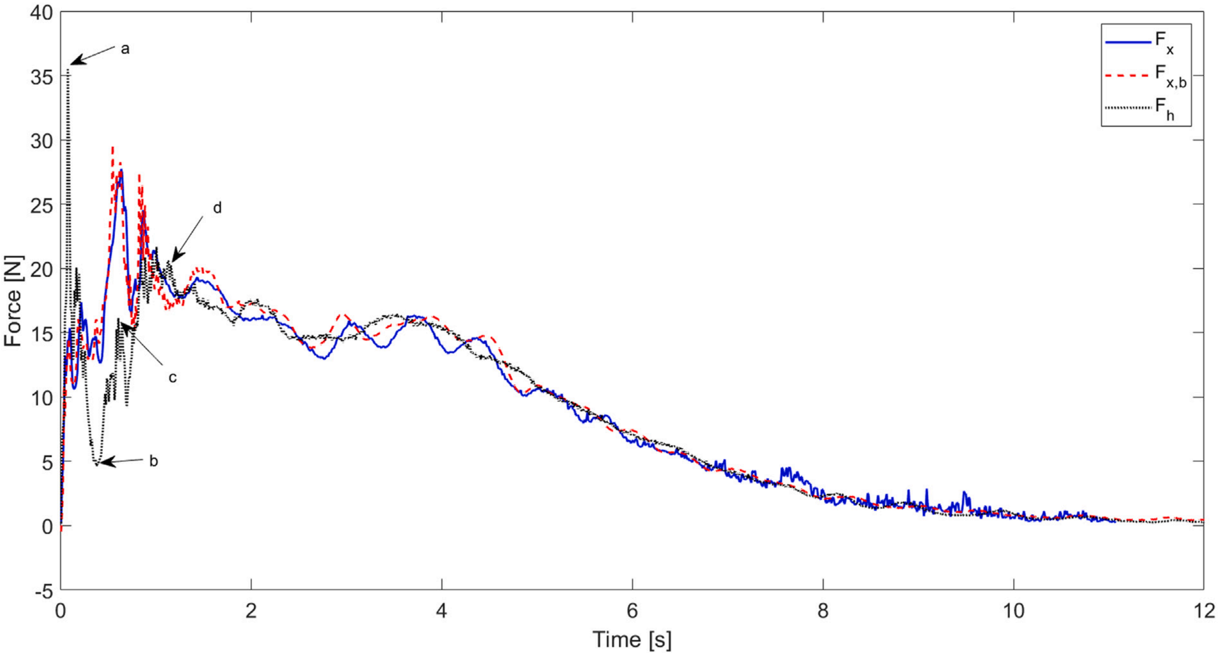

Fig. 10. Time series F_x, $F_{x,b}$ and F_h for the inundation of a $T = 23.5$ s trough-led wave on the h_{wall} = 0.25.

point [d] on Fig. 10). The quasi-static peak load, denoting the peak load after the reflected bore completely dissipates (for example Cuomo et al., 2010a) occurs at $t \approx 3.5$ s.

As discussed in Section 4.2 and this section, while the loading indicates impulsive forces are present in broken wave front impacts, as might be expected, the period of these waves is significantly shorter that ≈ 100 s at 1:50 scale may not be representative of earthquake generated tsunami at prototype. As shown in Fig. 6 and discussed in Section 4.1, waves that scale to tsunami-length periods at prototype did not break in this set-up.

4.4. *Overtopping volume*

Overtopping of coastal defences attacked by wind waves can be quantified by a total volume V_{tot} per unit width of wall [m^2]; by a mean overtopping discharge rate q_{av} per unit width [m^2 s^{-1}]; or a peak discharge q_{peak} [m^{2}s^{-1}]. For a single tsunami overtopping event, V_{tot} and q_{av} may be useful to relate to the damage rate on the landward side of the wall. q_{av} in particular may be used to determine the onset of phenomena such as scour, which is a major failure mode and strongly dependent on flow velocity. For the case of plunging scour, from

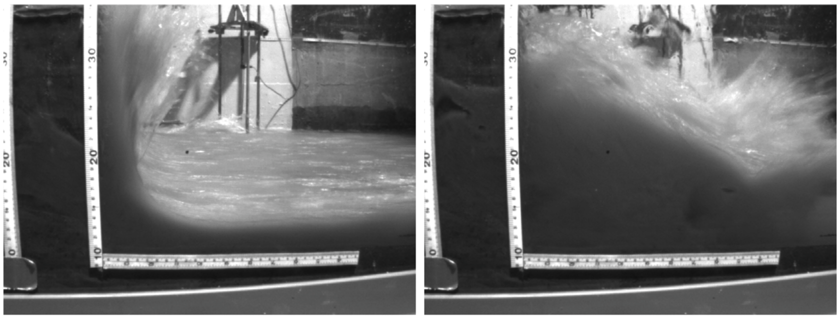

(a) Upward inflection of broken wave front. Image captured at $t \approx 0.08$ s.

(b) Collapse of deflected wave. Image captured at $t \approx 0.38$ s.

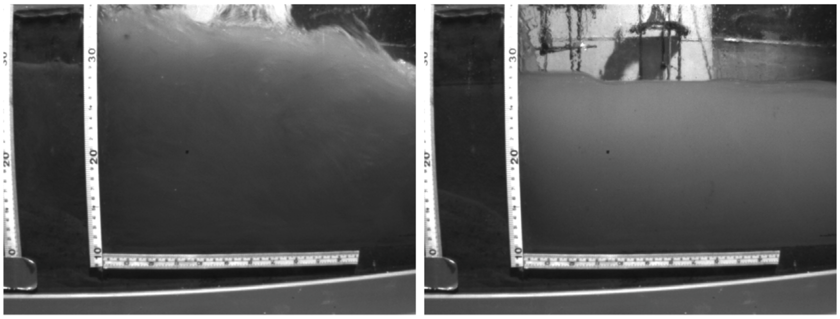

(c) Turbulent mixing. Image captured at $t \approx 0.61$ s.

(d) Quasi steady load. Image captured at $t \approx 1.01$ s.

Fig. 11. Relevant image stills of the main phases of a T = 23.5 s trough-led wave.

overtopping flows, ASCE (2022) provided an equation (Equation 6.12-4 therein) for the calculation of plunging scour depth that requires knowledge of q_{av}. V_{tot} and q_{av} may also help in understanding the potential effect of ponded water and the drainage time back to the sea, particularly if the overtopped wall remains structurally intact during the tsunami event (such as a 'level 2' event as described in Shibayama et al., 2013, or a barrier that is intended to provide 'partial impedance' of a tsunami as mentioned in ASCE, 2022). The design of return flow channels and enablers such as tsunami wall gates, may be aided by knowledge of expected V_{tot} from which return flow rates may also be inferred.

For this set up, in which each tsunami is a single distinct wave event, the total overtopping volume V_{tot} per unit width of the wall is recorded. This is recorded from the volume of water in the overtopping box at the end of each test, divided by the sampling width 0.1 m to give a volume per unit width. Of the two wall heights tested, most overtopping was observed on the smaller h_{wall} = 0.15 m, as expected. In these cases, the overtopping behaviour is 'green water', meaning that the wave is generally coherent and unbroken during the overtopping phase. The largest V_{tot} is observed when an unbroken T = 20 s trough-led wave inundates and overtops the h_{wall} = 0.15 m wall (as shown in Fig. 19 and discussed in detail in the next Section 4.5). For shorter period waves that break before inundating the wall, some of the initial overtopping is 'white water', and these generally lead to lower values of V_{tot}. However, it is highlighted that the majority of breaking waves were tested against the larger h_{wall} = 0.25 m. Such events tend to produce overtopping from the broken leading edge of the wave inundating the wall and being deflected vertically, before collapsing onto the crest with some remaining shoreward momentum resulting in overtopping. A typical example is given in Fig. 11, which shows the inundation of a T = 23.5 s trough-led wave. In this case, the inundation height at the wall h_a is not greater than the crest freeboard R_c, so overtopping occurs mostly through the collapse of the broken front onto the crest, and therefore the V_{tot} is low.

Of most use to the design engineer is if V_{tot} is related to the incoming characteristics of the overtopping wave. This may include the wave period T, the time duration of overtopping t_o and the upstream head height H_1 (the height of water at seaward face of the wall h_a - R_c). When V_{tot} is plotted against these inundation characteristics, (Fig. 12), there is no observable trend with T, but a clear positive correlation is observed instead but with t_o. The correlation with H_1 is weaker, and so it can be implied that the shape of the wave is the main driver of V_{tot}. This suggests that the longer the time for which $h_a > R_c$ (i.e., there is a positive head H_1 over the front face of the wall), the greater V_{tot}. To investigate further, the integration of positive H_1 with t is given in Fig. 12d. This does show a positive correlation, for the h_{wall} = 0.15 m data. However, for the h_{wall} = 0.25 m wall, it is weak likely because the nature of the overtopping is dominated by the collapsing broken wave as described in the previous paragraph.

This is particularly clear in the case of the six V_{tot} data points located well above the rest at ≈ 0.1, where although H_1 is not relatively large for these waves, the time duration of overtopping (t_o) is. That is to say, the crests of these waves are relatively long.

The discharge distribution of a storm wave overtopping a wall is generally characterised by a maximum discharge at the leading edge that is significantly larger than the time-averaged discharge. For the case of a long tsunami-like wave, the overtopping discharge is likely much more like a time-varying weir flow, or a storm surge overflow scenario. A reasonable overtopping hypothesis is that of similarity to a flow over a rectangular broad-crested weir. Flows on the seaward side of the wall will be sub-critical. If frictional energy losses over the length of the crest are ignored, a transition to critical flow will occur given sufficient length of crest. Upon reaching the landward edge, the flow will become supercritical. When analysing overtopping behaviour, the average discharge per unit width of wall q_{av} is usually presented as relative discharge rate, $q^* = \frac{q_{av}}{\sqrt{(gH_i^3)}}$ as a function of relative crest freeboard $R_c^* = \frac{h_{wall}}{H_i}$, where H_i is the incident wave height [m]. This

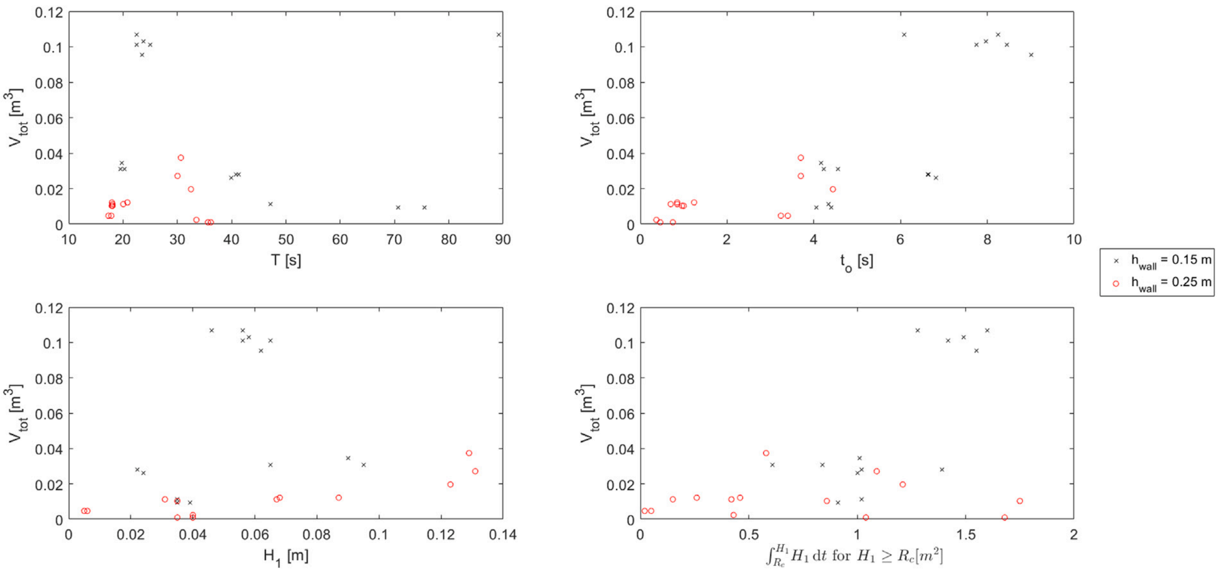

Fig. 12. V_{tot} as a function of T[s], t_o [s], the overtopping head height H_1 [m] and $\int_{R_c}^{H_1} H_1\,dt$ for $H_1 \geq R_c$ [m^2].

allows engineers to determine whether for a given relative crest height, q^* will be greater than standard empirical predictor equations that are widely used in current design guidance such as EurOtop (Van der Meer et al., 2018). In EurOtop, the scenario which this experiment is most similar to is that of a non-impulsive inundation for a simple vertical wall with an influencing foreshore (shallow water wave conditions). For this scenario, EurOtop recommends Eq. (9) with the more conservative Eq. (10) to be used in design and safety assessments.

$$\frac{q}{\sqrt{(gH_i^3)}} = 0.05\exp(-2.78\frac{R_c}{H_i}) \tag{9}$$

$$\frac{q}{\sqrt{(gH_i^3)}} = 0.062\exp(-2.61\frac{R_c}{H_i}) \tag{10}$$

By plotting q^* as a function of R_c^*, the effectiveness of these equations in modelling the recorded data can be determined (Fig. 13). Though clearly Eurotop is not intended for tsunami inundations, the comparison is of use as it provides a reference against a well-understood and related phenomena (wind wave overtopping) against which tsunami overtopping can be compared.

When compared with Eqs. (9) and (10), the recorded overtopping is reasonably well described using $q_{av} = \frac{V_{tot}}{T}$, with some significant underestimation for a group of waves at $R_c \approx 1.67$ in particular (Fig. 13a). This relates to waves whose overtopping duration is relatively long, as discussed in Fig. 12 indicating that the EurOtop code, which is designed for and based upon windwave overtopping, with wide variation of wave height within a test series (often of 1000 waves), does not apply for long period tsunami overtopping. This is even clearer when $q_{av} = \frac{V_{tot}}{t_o}$. By dividing by t_o, the duration of overtoppping is directly accounted for, and Fig. 13b shows that wind wave approach severely underestimates the overtopping of a tsunami. This is not surprising considering the differences of the two phenomena, wind waves often overtop as white water, and over a relatively short duration. Tsunami as shown here, overtop as green water and over a significantly longer duration than wind waves. They are more analogous to an open channel gravity flow (such as a time-varying weir flow) with some added momentum from the velocity of the incoming flow.

4.5. Effect of overtopping on time history of force

Though the maximum horizontal forces appear not to be influenced by overtopping (Fig. 6), a number of different characteristics in the time history of the loading are observed when a long wave overtops the wall. These observations are now discussed in terms of the integrated pressure readings F_x and the horizontal body force $F_{x,b}$. As described in Section 3 the 0.1 m wide section of the wall is cantilevered on a 3-axis load cell. In this set-up, it can respond in the x direction under horizontal loads.

Starting with TL20 wave (T = 20 s), the time series loading of $F_{x,b}$ and F_x are shown on Fig. 14. There are three identifiable loading phases. (1) upward deflection of the wave front $t \leq \approx 1$ s, which is visualised by an image captured by the high-speed video camera (Fig. 15a). The error of the correlation between the loading recorded by the data acquisition system (which record the load cell and pressure transducers), and the high-speed video cameras is in the order of ± 0.02 s. This is followed by phase (2) which begins with the overtopping between $t \approx$ 1–5.5 s (imaged on Fig. 15b), and finally phase (3), a hydrostatically dominated receding phase (15c).

In the first phase, $F_{x,b}$ and F_x are well correlated, both reaching a maximum value greater than F_h at $t \approx 1$ s indicating there is some added momentum in the inundation (this remains the case until midway through phase 2). Overtopping occurs during the latter stages of phase 1 of the inundation, in so much as the collapsing wave front first spills over the landward side of the crest. The water height in front of the wall H_a does not exceed R_c at this point. This occurs some moments later, initiating overtopping flow.

Overtopping flow in phase 2 begins at $t \approx 0.85$ s and is identified by F_x deviating below $F_{x,b}$, due to the presence of a hydrodynamic drag load, which can only be measured by the load cell, not the pressure transducers. F_x remains > F_h at this point, indicating momentum in the X direction remains. This can also be seen in less smooth response of the $F_{x,b}$ trace between $t \approx$ 0.84–2.37 s, which when observed in the high speed video, correlates with highly turbulent overtopping flow (such as imaged in Fig. 15b). Beyond this point the overtopping flow in phase 3 becomes less turbulent. F_x converges with F_h at $t \approx 2.37$ s, indicating the load on the front face of the wall is now purely hydrostatic, while $F_{x,b}$ begins to converge at $t \approx 6.5$ s, when overtopping ceases, and there is no longer a drag component of force (as imaged in Fig. 15c).

Now F_x, $F_{x,b}$ and F_h as a function of t for a $T \approx 40$ s troughled wave inundation is discussed. This inundation, which also includes overtopping, is also describable in three phases (Fig. 16).

The initial 2 s is characterised by the inundation of a partially broken aerated incident wave front and a turbulent reflecting bore. These are shown in images Fig. 17a and b. The initial inundation in

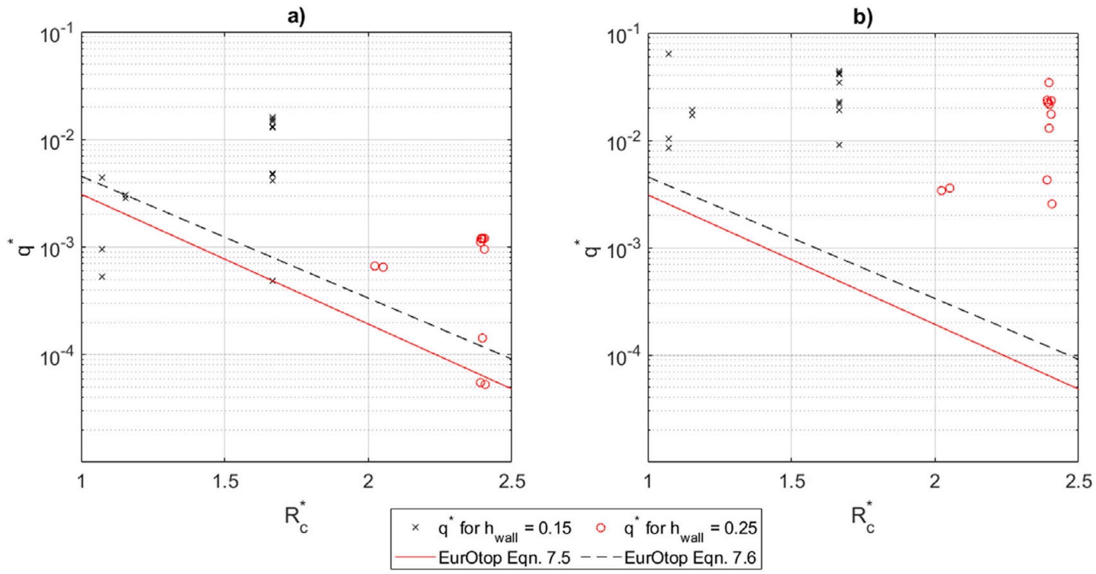

Fig. 13. (a) q^* as a function of R_c^* for each wall and the empirical prediction Eq. (11) (7.5 in Eurotop), here $q_{av} = \frac{V_{tot}}{T}$. And (b), q^* as a function of R_c^* for each wall and the empirical prediction Eq. (10) (7.6 in EurOtop). Here $q_{av} = \frac{V_{tot}}{t_o}$.

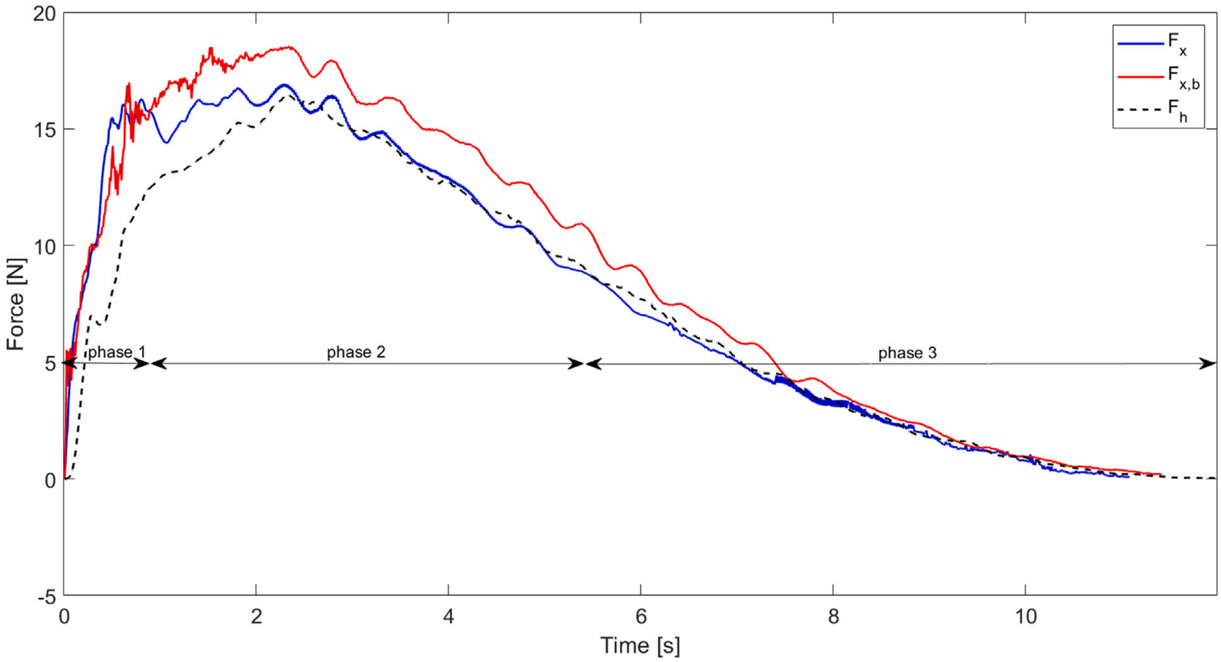

Fig. 14. F_x, $F_{x,b}$ and F_h as a function of t for a $T \approx 20$ s N wave.

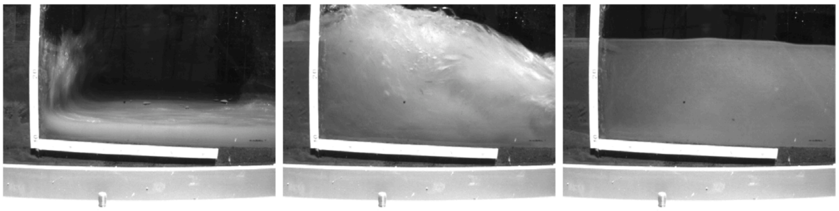

(a) Image at $t = 0.1$ s (b) Image at $t = 0.85$ s (c) Image at $t = 5.5$ s

Fig. 15. Image stills of key points of the TL20 wave inundation of which the loading profile is shown in Fig. 14.

phase 1 occurs between 0 to 3 s. Here F_x and $F_{x,b} \approx F_h$. As this wave has a shallower steepness, much of the initial inundation energy is reflected in a reflecting bore (Fig. 17b), rather than vertically upward as in the previous wave discussed. By the time overtopping occurs in

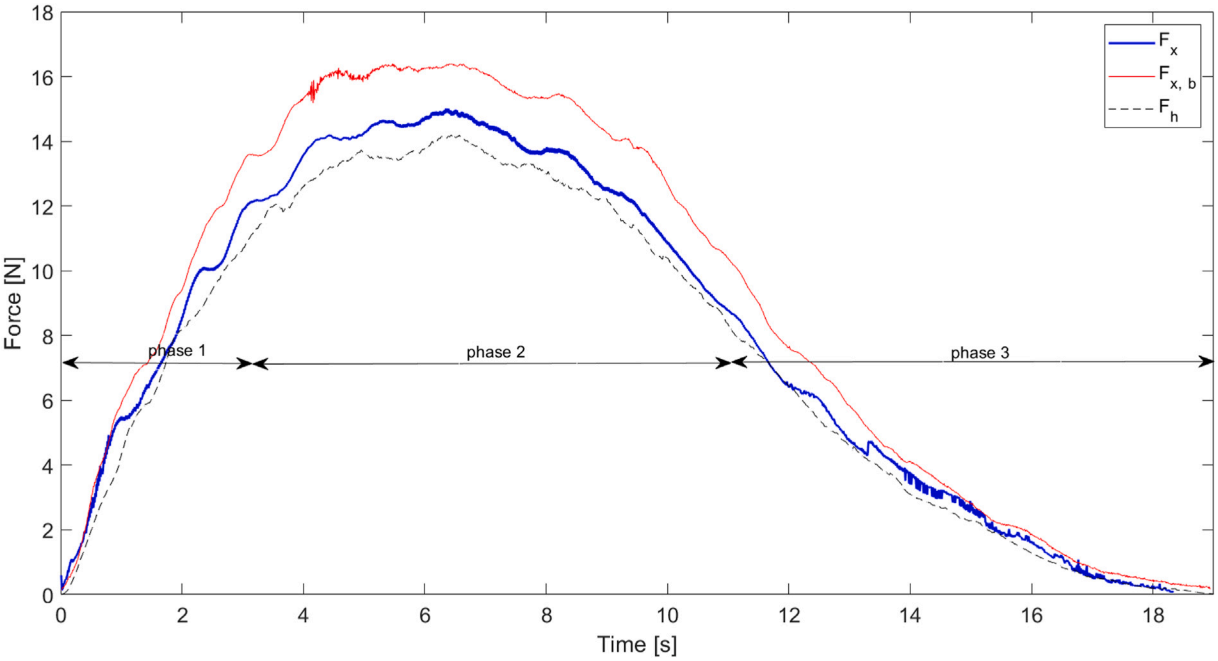

Fig. 16. F_x, $F_{x,b}$ and F_h as a function of t for a $T \approx 40$ s N wave.

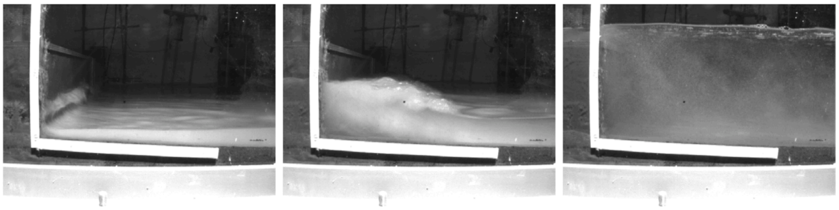

(a) Image at $t = 0.16$ s (b) Image at $t = 0.64$ s (c) Image at $t = 5.68$ s

Fig. 17. Image stills of key points of the TL40 inundation of which the loading profile is shown in Fig. 16.

phase 2 (from $t \approx 3$ s–11 s), the flow is not particularly turbulent (imaged in Fig. 17c). Overtopping causes an increase in $F_{x,b}$ due to drag. There is also evidence of higher frequency response in $F_{x,b}$ due to frictional effects of the overtopping flow on the wall crest which excite a higher frequency vibration response in the cantilevered well segment. F_x remains only slightly above F_h during this phase, due to $h_a > R_c$. Convergence of $F_{x,b}$ and F_x on to F_h occurs after overtopping ceases at 11 s and $F_x \approx F_x \approx F_h$ during the 3rd, receding phase.

Finally the loading profile of F_x, $F_{x,b}$ and F_h as a function of t for a $T \approx 20$ s crest-led wave is discussed. In this case the wave front is not broken and contains little trapped air. The loading profile time-series is similar to the previous waves with a clear three-phases of inundation (Fig. 18). The classification of the inundation phases include the impulsive, overtopping and recession phases, with caveats.

In phase 1, $F_{x,b} > F_x$ from $t \approx 2$ s, indicating some momentum is transferred to the wall during the initial impingement, but that this is not related to impulsive inundation forces (Fig. 19a). Overtopping begins at ≈ 2.1 s (phase 2). As can be seen in the previous waves, the $F_{x,b}$ time series trace becomes noisier when overtopping initiates, indicative of the frictional drag force applied along the crest that excites a vibration response in the cantilevered wall segment. While $F_{x,b}$ remains $> F_x$ during the initial stages of overtopping, an aerated nappe forms on the landward side of the wall from the overtopping flow and advances towards the rear toe of the wall. This trapped water volume on the landward side of the wall reduces the resultant body force on the front face of the wall and $F_{x,b}$ converges to F_h by $t \approx 4.6$ s.

The measurement of the body forces $F_{x,b}$ demonstrates the influence of hydrodynamic drag on the wall present during overtopping. While the time-series loading profile does appear variable depending on the incoming wave characteristics and overtopping characteristics (be it turbulent or green water), the maximum $F_{x,b}$ recorded is only marginally greater than F_h. Taking into account standard design safety factors (e.g., for vertical and composite breakwaters in Japan a safety factor against sliding failure from wind waves of 1.2 times the maximum F_h is suggested by Goda, 2010), the additional horizontal force from overtopping may be considered negligible as the overall maximum force is approximately equal to hydrostatic with a reasonable factor of safety. The presence of higher frequency of vibrational loading superimposed on the horizontal body force during overtopping may have significance in some design scenarios. Natural frequencies of concrete gravity walls are unlikely to be within this range of frequency, but this should be considered, especially for smaller individual component structural members.

4.6. *Comparison with existing prediction equations*

The results discussed in Section 4.1 show that $F_x/F_h \approx 1$ for $T > 40$ s (Fig. 6). The slow pulsating inundations indicate that the tsunami-length waves may be considered as very long period clapotis at the wall. In which case, the equations suggested by Hiroi (1920), Sainflou (1928), Goda (2010) appear most suitable to describe the imparted force (respectively, Eqs. (1); $p_{av} = 1.5\rho g H_D$, (2); $P = (p_2+\rho g h)(H_D+\delta_0)$) and (3); $p_{max} = 2.2\rho g a^+$).

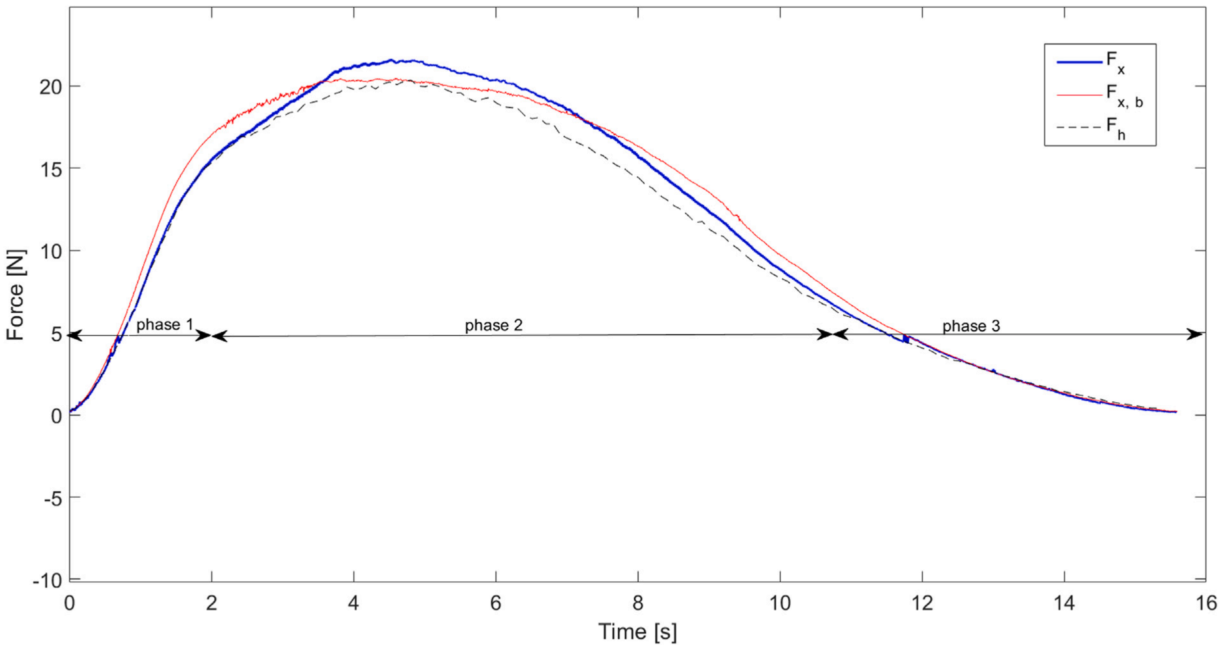

Fig. 18. F_x, $F_{x,b}$ and F_h as a function of t for a $T \approx 20$ s elevated wave.

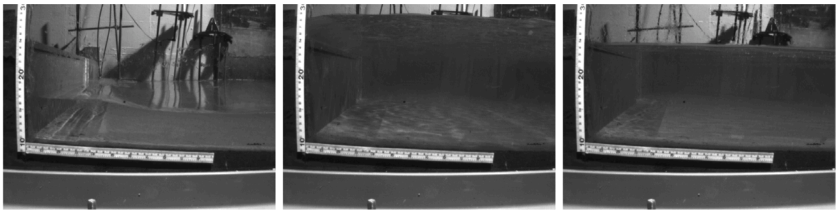

(a) Image at $t = 0.71$ s (b) Image at $t = 8.71$ s (c) Image at $t = 10.5$ s

Fig. 19. Image stills of key points of an TL20 wave inundation.

The recorded force F_x at the wall, from the integration of pressure is now compared against the predictions given by each of the above equations $F_{x,predicted}$. In applying these equations to the waves tested a value of incident wave height H_i is required. Starting with Eq. (2), for the long waves tested, the value $\delta_0 \to 0$ due to the very long wavelength λ. The reflecting coefficient = 1 for a vertical smooth wall. The toe of the wall tested is above mean water level MWL (an onshore wall) and the water depth in which H_i is defined at is 1 m (the toe of the flume bathymetry) for these waves. In effect $H_i = a^+$.

There is ambiguity in the literature of what H_i represents (d' Angremond and van Roode, 2004) and its application to tsunami is unclear. Indeed the definition of H_i (analogous to a^+ in this case) is non-trivial for very long waves (McGovern et al., 2018), and may not fully account for reflected wave energy or shoaling of such waves. Therefore, $H_i = h_{max}$ (the maximum height of water recorded at the wall) is also tested for each equation.

The comparison of F_x versus $F_{x,predicted}$ is shown in Fig. 20. The left column shows F_x versus $F_{x,predicted}$ for each equation with $H_i = a^+$ and the right column with $H_i = h_{max}$.

Where $H_i = a^+$ the equations are very good for $F_x \leq 11$ N. The good performance is due to the value of a^+ being effectively unchanged by insignificant shoaling between its definition point $X = 65.6$m and the wall. Those waves that are underestimated by the equations are ones which overtop and have larger impulsive components where $T < 40$ s.

While the equations perform well for the waves that do not appreciably shoal, they grossly underestimate for shorter period waves (with $F_x \geq 11$ N), some of which break and overtop. While Eq. (1) and (3) do not account for shoaling, Eq. (2) does account for an increase in H_i at the wall through the δ_0 term. Its poor performance suggests that very long waves and tsunami are not described well by trachoidal theory of which the equation considers, as might be expected.

Now, setting $H_i = h_{max}$ (right column, Fig. 20) the equations give consistent conservative overestimates by a factor of approximately 50% (Eq. (1)) and 120% (Eqs. (2) and (3)). This is to be expected given the use of h_{max}, which is always $\geq H_i$ in these tests. The implication is that the force at the wall from a tsunami is dominated by the hydrostatic force imparted by h_{max}. Eq. (1) appears suitable to give conservative estimates and the multiplying coefficient need only be tuned to a desired safety factor.

4.7. *Correlation of force to wave parameters*

As discussed in Section 4.1, the resultant force F_x on the front face of the wall is well described by the hydrostatic force from h_{max}. Of additional benefit to the coastal engineer is the ability to link F_x to a characteristic of the waveform, usually a^+. This follows the ASCE 7-22 Tsunami Loads and Effects code (ASCE, 2022) where the a^+ of an incident tsunami is defined offshore at the 100 m depth contour. Relating F_x to a^+ requires a good understanding of the shoaling characteristics of tsunami. The amplitude of the incident tsunami wave will change as it enters shallower coastal water due to shoaling effects and interference from reflections. Therefore, to understand how shoaling affects the wave, the correlations between the value of h_{max} (which as above, is shown to have a strong correlation with the recorded F_x) and the potential influencing parameters of the wave are now investigated.

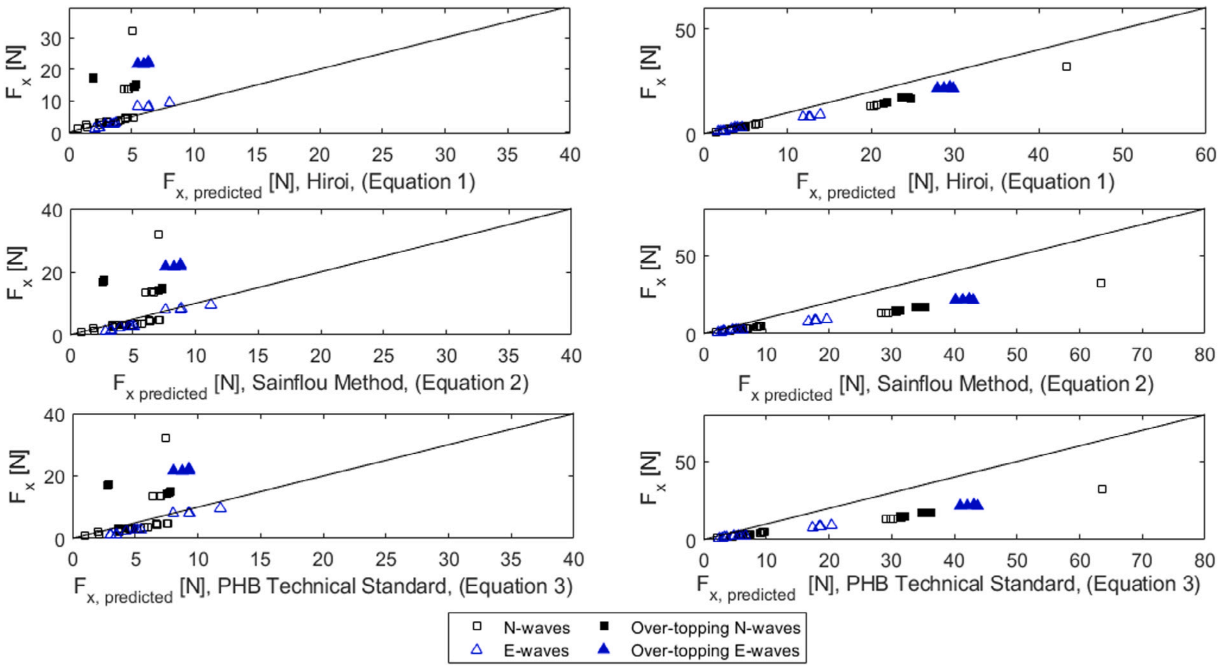

Fig. 20. F_x versus $F_{x,predicted}$ from Eqs. (3), (1) and (2) with $H_i = a^+$(left column) and with $H_i = h_{max}$ (right column).

Fig. 21 shows correlation plots of h_{max} with the offshore value (as defined at the bathymetry toe $X = 65.5$ m) of T, a^+, a^- (negative amplitude, for trough-led waves), wave celerity C, wave potential energy E_p, defined using the integral method described in McGovern et al. (2018), wavelength λ, d and wave steepness λ/a^+. There are no correlations between C and d with h_{max}. The negative correlation with T is due to the increasing shallowness of the incident wave with increasing T, as clearly observed in λ/a^+. a^+ is positively correlated as expected, and a similar though weaker correlation is observed in a^-. This is likely a reflection of the symmetry between the trough and crest sought in the majority of the trough-led waves (namely those in Table 1). E_p shows a negative correlation, which though quite weak, can infer that the distribution of energy in the wave, not just its absolute value, is important. This is also observed in McGovern et al. (2018), where the shape of the wave, described by λ/a^+ is shown to have a significant influence on its the runup. The correlation between F_x and λ/a^+ is very good.

In McGovern et al. (2018) the runup R of a tsunami wave on a constant slope beach is shown to correlate best with a parameter called Relative Slope Length (RSL = $\frac{\lambda sin(\alpha)}{d}$). The RSL accounts for the shoaling characteristics of the tsunami by considering the ratio of the incident λ, to the wetted length of sloping bathymetry the wave travels over before impinging on the shoreline L_b (the reciprocal of $\frac{sin(\alpha)}{d}$). The amount of shoaling that the tsunami undergoes is directly related to its eventual R and for very long tsunami-length waves, R/a^+ is shown to be equal to ≈ 1. Following from McGovern et al. (2018), Fig. 22 presents the increase in the free surface height η between the bathymetry toe at $X = 65.6$ m where the wave characteristics are defined, and the offshore edge of the wall at $X = 84.6$ m (where h_{max} is defined) as a function of a^+, T, λ, d, C_{exp}, $\frac{\lambda sin(\alpha)}{d}$. Minimal shoaling is observed for waves of T and RSL of ≥ 100, (a similar range as observed in McGovern et al., 2018 for $R/a^+ \approx 1$). Therefore, h_{max} can be considered a function of the variables in Eq. (11), which includes RSL.

$$h_{max} = f\left(a^+, T, \lambda, d, \frac{\lambda sin(\alpha)}{d}\right) \tag{11}$$

The following hypothesis is postulated. As also shown in McGovern et al. (2018), very long waves are not subject to significant shoaling and as such behave similarly to a slosh (notwithstanding that they are not bounded in a container in motion) or seiche over the bathymetry tested. This is a primary observation from the data presented and leads to the force recorded at the wall being dominated by the hydrostatic component. A similar finding was given by Foster et al. (2017) who show the force on a onshore structure to be well described by hydrostatic theory, with some additional momentum. Whether a tsunami may break or not may be dependent on the RSL which accounts for the length of the wave and the slope and length of the approaching bathymetry. In these experiments, as well as in the experiments described in McGovern et al. (2018), Foster et al. (2017) who use the same flume and tsunami simulator, and those described in McGovern et al. (2019) who use a larger tsunami simulator in a 4 m wide 70 m long flume, shoaling does not lead to breaking for the tsunami-length waves generated.

5. Discussion

The analysis of the data presented shows that tsunami inundation forces with vertical walls are hydrostatic dominated and generally not greater than 1.2 F_h. Changes in hydrodynamic drag force and vertical forces from overtopping and buoyancy are observed over the inundation of the wave, overall however, these are relatively small in comparison to the dominant landward hydrostatic load. In the case where the wave front is broken, (relating to short period waves) short-lived impulsive forces may be recorded at the wall. However, wave breaking does not occur for $T \geq 40$ s, suggesting that in the current laboratory conditions bore induced impulsive forces are not relevant to tsunami-length wave inundations. This leads to the question of in what conditions a tsunami may be bore led, and how this should be tested in laboratory conditions. It is usually modelled using the dam-break method, however, this might not account for the temporal variation of wave parameters during an inundation of a long period wave that shoals and/or fissions into an undulating bore by the time of inundation. Namely these are the changes in instantaneous free-surface height and the fluid velocity during the inundation time. Tsunami wave fissioning into successive bore fronts may occur over long and shallow nearshore bathymetries. These bore fronts overlie the long period wave and as shown in this study, their impacts may only dominate the loading for very short periods in comparison to the inundation of the main tsunami wave they override. In addition, McGovern et al. (2019)

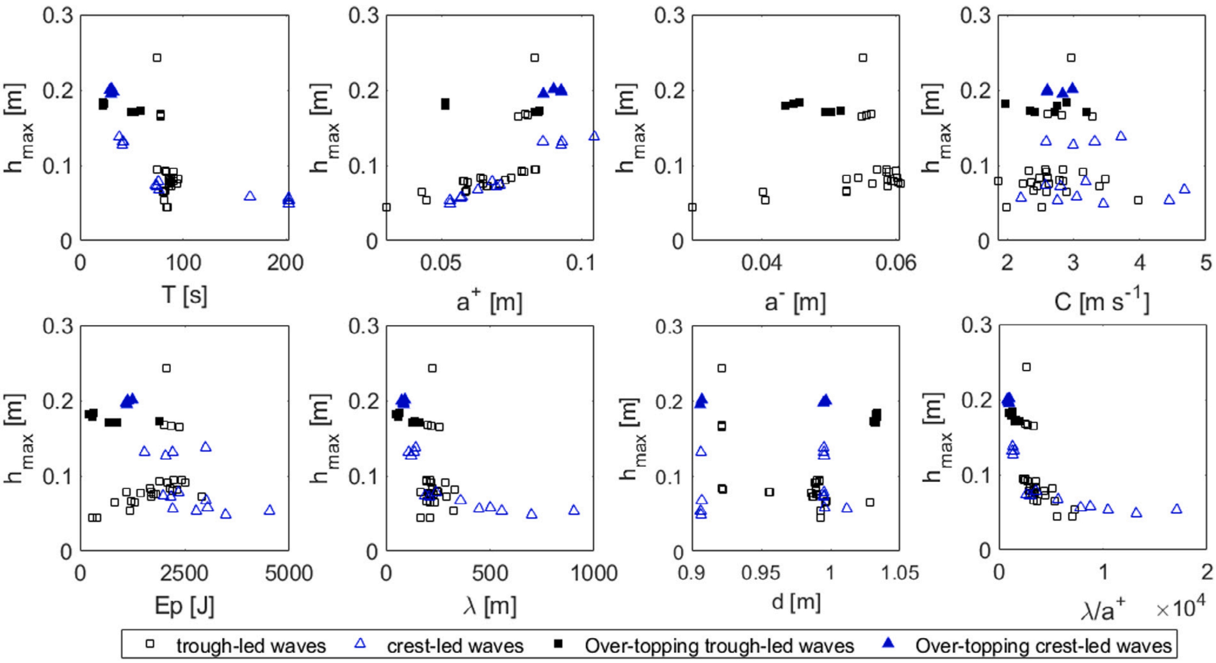

Fig. 21. Correlation plots variables potentially influencing the recorded h_{max} for the trough and crest-led waves tested.

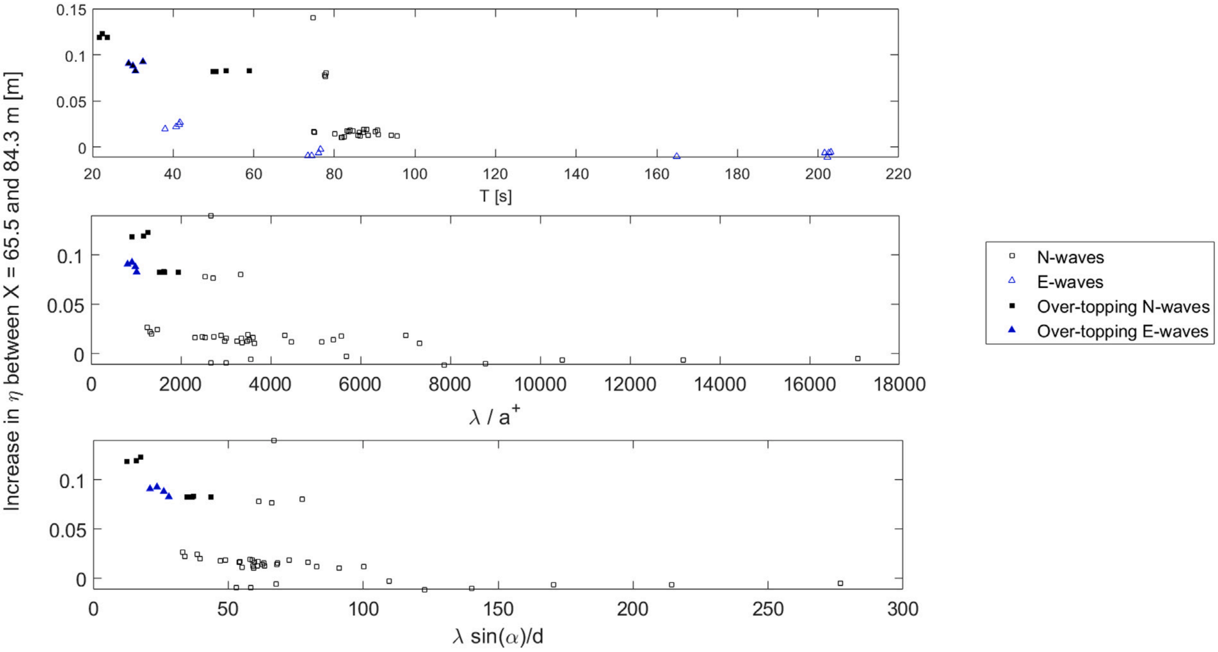

Fig. 22. Increase in η between X = 65.6 and 84.3 m (front face of wall).

show the maximum velocity both on shore and offshore of a Froude-scaled tsunami occurs at $\frac{2}{3}\eta$, and this is also observed in field surveys (ASCE, 2022). Whereas the dam break method generates an initial U_{max} and η_{max} followed by a gradual decrease in both parameters.

The results in this paper for short waves and studies of tsunami bore forces such as Kihara et al. (2015), Nouri et al. (2010), Shafiei et al. (2016) and Al-Faesly et al. (2012) indicate that bore induced hydrodynamic forces, while potentially very large, are also very short-lived. For large, massive concrete gravity walls, for example, such very short-lived pressures may be regarded as a spatially localised phenomenon, whose temporal scale is much shorter than the structural response of the upright wall sections (e.g., Goda, 2010). Field data of tsunami induced wall failure is rare, and usually failure modes may only be analysed in retrospect. The majority of such data is drawn from post-TET field surveys and as such, it is hard to delineate the effects of the inundation with the return flow. Even so, these field surveys suggest that many failure modes are related to phenomena that occur over longer periods than impulsive inundations. These include foundation scour, structural sliding and overturning, and suction caused by lift force on armour layers during overtopping (EEFIT, 2011, EEFIT, 2013, Chock et al., 2013, Mori and Takahashi, 2012 and Fraser et al., 2013). The implication is that consideration of the non-breaking quasi-steady characteristics of tsunami wave inundation is important in tsunami wall design.

Goda (2010), in describing the history of vertical seawall construction references a general paradigm for storm waves of one that the design waves are relatively large and steep in the water depth that many walls are situated in, meaning breaking generally occurs and must, therefore, be considered in design practice. Due to the absence of tsunami force measurements at prototype walls, the engineer may have conservatively relied on laboratory scale analogues of tsunami using breaking solitary waves and dam-break bores (e.g., Nouri et al., 2010, Robertson et al., 2013 and Kihara et al., 2015). Further, a notable problem of design methods using bore velocities is that such velocities are seldom available. However, tsunami generation methods that produce Froude-scaled very long wave T such as those of Rossetto et al. (2011), Goseberg et al. (2013), Schimmels et al. (2016), Sriram et al. (2016), McGovern et al. (2018), which account for the inherent shallowness and long period of tsunami waves, rarely if at all present wave breaking or impulsive loads. This is an important observation of this paper and of Foster et al. (2017), for the case of onshore structures. Impulsive effects may be somewhat rarer than might be implied by solitary wave and dam break studies. Further, the solitary and dam break methodologies while clearly suitable for the bore generation, may not be as capable of accounting for important long period inundation, overtopping, and correct tsunami wave scaling of the temporality of flow velocities and inundation heights over the full inundation of a wave.

The main results of these experiments (pressures, forces, and overtopping rates and volumes) can be scaled directly using the Froude criterion. As discussed in Section 3.1, there are potential scale effects in Reynolds (viscosity) and Weber (aeration). These seldom alter the main outputs listed above. The results presented are recorded over an idealised bathymetry. The selection of a smooth constant slope angle in the nearshore region enables a general applicability to the results, consistent with general hydraulic design practice. Further as the main driving excitation are tsunami waves having wavelengths in prototype of the order of hundreds of metres, small variations of bed slope, roughness or level will have consequentially small effects on the response. To address this limitation, the experimental data set may inform the numerical treatments of tsunami overtopping, which would expand the variables tested, and eventually enable more complex bathymetries to be studied. The model sea walls used in these tests scale to prototype vertical tsunami defence walls of typically wide crown widths. Prototype walls of lesser crown width may only differ in the drag force imparted as the hydrostatic loads and overtopping are determined primarily by the height of water on the seaward face.

The design engineer may from these results expect hydrostatic and overtopping loads to dominate temporally during tsunami inundation of a wall. From this they might also easily calculate the maximum expected moments for a given wall and tsunami inundation height. These findings give the engineer the input variables (force) that can be used in standard stability analyses of sliding and overturning failures. Further, the effect of the long period of hydrostatic loads and overtopping flow should also be considered in those structural and geotechnical responses that are sensitive to the load duration. Wave overtopping adds additional drag load that occurs due to the flow over the top surface of the wall. This may lead to frictional forces and likely lift forces occurring on the top surface; as has been observed in the field to lift concrete capping members from walls as a failure mode (e.g., Chock et al., 2013). Walls should also be designed with the possibility of significantly larger instantaneous forces, though it is unlikely that these forces will excite large mass gravity structures dynamic responses.

A well-documented failure mode of sea walls during the TET was that of foundation scour at the landward toe of the walls from overtopping flows (e.g., EEFIT, 2011, EEFIT, 2013 and Chock et al., 2013). Scour depth and intensity is sensitive to flow velocity and inundation time, as observed by McGovern et al. (2019) for flow past partially blocking structures. Further studies of overtopping flow and landward toe and foundation scour would be useful. Measurements of overtopping flow of significantly longer periods than achieved in this paper would be useful in which the time dependent vertical, horizontal and momentum forces and velocities of the overflow could be analysed.

6. Conclusions

This paper describes a set of large scale experiment of very long wave inundations with a vertical sea wall. Trough and crest-led waves of periods between 6.5–240 s model (46 - 1697 in prototype at nominal scale 1:50) are generated in a 100 m long flume in 1 m water depth using a Pneumatic Long-wave Simulator (Tsunami Simulator). They travel up a 1:20 slope towards a vertical wall of either 0.15 m or 0.25 m height. It is observed that wave periods ≥ 40 s do not impart significant impulsive forces, and the resultant force at the wall is not observed to be greater than 1.2 times the hydrostatic force. The reason for this is waves of this length do not shoal enough to break. The time series loading profiles are observed to show increases in horizontal body force due to momentum and drag. However, the values of these increases over the hydrostatic load are relatively small. These observations imply the modelling of tsunami forces from bore inundation may apply only rarely. The results presented compare well with existing prediction equations based on hydrostatic force. While the definition of the incident wave height to input into the hydrostatic equations remains problematic, the engineer may apply a desired multiplying coefficient of a factor of at least 1.2 to account for any added pressure and momentum and the factor of safety intended.

CRediT authorship contribution statement

David J. McGovern: Conceptualisation, Methodology, Formal analysis, Investigation, Writing – original draft, Project administration. **William Allsop:** Conceptualisation, Methodology, Writing – review & editing, Resources, Supervision. **Tiziana Rossetto:** Conceptualisation, Methodology, Writing – review & editing, Resources, Supervision, Project administration, Funding acquisition. **Ian Chandler:** Conceptualisation, Methodology, Writing – review & editing, Resources.

Declaration of competing interest

The authors declare that they have no known competing financial interests or personal relationships that could have appeared to influence the work reported in this paper.

Data availability

Data will be made available on request.

Acknowledgements

This work is fully funded by the European Research Council project “URBANWAVES” [Starting Grant: 336084]. The experiments use the 2nd generation Tsunami Simulator developed and constructed by HR Wallingford and operated onsite at HR Wallingford. The input of other researchers to these experiments is gratefully acknowledged. In no specific order: Dr Andrew Foster, Dr Crescenzo Petrone and Dr Tristan Robinson, Dr Ignacio Barranco Granged of HR Wallingford and the following post graduate students Ms Daniela Figueroa Ibarra and Mr Oliver Cook of University College London.

Appendix A. Test conditions

Table A.1 gives the test conditions and the standard deviations of the mean of repeated tests, where appropriate.

Fig. A.1 shows the propagation of a TL80 s wave down the flume from selected gauges. It shows the wave definition point at $X = 65.6$ m and the seaward toe of the wall at $X = 86.4$ m. Destructive interference is observed and an in-depth analysis of wave propagation, reflection and interference is given in McGovern et al., 2018 for the same flume.

Table A.1
Test Conditions in Full.

Wave type	Target T [s]	T [s]	a^+ [m]	a^- [m]	C_{exp} [m/s]	E_p [m]	λ [m]	d [m]	No. of repeats No. of repeats
TL	TL20	22.64	0.05	−0.04	2.54	278.39	2.54	1.03	3
σ	1.03	0.00002	0.001	0.5	54.18	0.5	0.0003		
TL	TL50	53.17	0.08	0.05	2.67	1057.41	2.67	1.03	4
σ	4.02	0.001	0.001	0.39	563.66	0.39	0.001		
TL	80	75.05	0.08	−0.06	2.7	2338.45	2.70	0.99	2
σ	0.16	0.0003	0.001	0.19	138.55	0.19	0.001		
TL	TL80	77.81	0.08	−0.06	2.91	2180.77	2.91	0.92	3
σ	0.17	0.0002	0.001	0.35	195.36	0.35	0.0003		
TL	–	80.93	0.044	−0.04	3.44	1002.74	3.44	1.01	2
σ	1.11	0.001	0.0002	0.76	264.23	0.76	0.03		
TL	–	85.64	0.044	−0.04	3.44	1002.74	3.44	1.01	2
σ	0.17	0.0002	0.001	0.35	195.36	0.35	0.0003		
TL	–	83.16	0.079	−0.059	2.33	1887.83	2.33	0.99	3
σ	3.99	0.001	0.001	0.41	319.09	0.41	0.001		
TL	–	86.71	0.074	−0.059	2.70	2185.14	2.70	0.99	2
σ	0.66	0.002	0.001	0.12	44.60	0.12	0.0002		
TL	–	94.17	0.071	−0.56	2.23	1743.76	2.23	0.99	1
TL	–	75.05	0.08	−0.06	2.70	2338.45	2.70	0.99	2
σ	0.16	0.0003	0.0010	0.19	138.55	0.19	0.001		
TL	–	82.20	0.059	−0.053	2.50	1,258.42	2.50	1.00	2
σ	0.30	0.0001	0.0001	0.14	60.47	0.14	0.0005		
TL	–	77.81	0.079	−0.056	2.91	2180.77	2.91	0.92	3
σ	0.17	0.002	0.001	0.35	195.36	0.35	0.0003		
TL	–	74.71	0.083	−0.055	2.97	2056.43	2.97	0.92	1
TL	–	93.28	0.064	−0.053	2.98	2003.51	2.98	0.92	2
σ	3.29	0.0005	0.0012	0.70	460.70	0.70	0.0003		
TL	–	86.90	0.066	−0.059	2.82	2140.66	2.82	0.99	3
σ	1.28	0.001	0.001	0.50	673.76	0.50	0.002		
TL	–	88.66	0.058	−0.06	2.35	1413.33	2.35	0.97	3
σ	1.82	0.001	0.001	0.49	295.52	0.49	0.02		
TL	TL160	163.44	0.039	−0.037	2.37	1241.84	2.387	0.993	2
σ	3.42	0.001	0.001	0.959	497.07	0.959	0.001		
TL	TL200	210.10	0.039	−0.039	2.17	1266.54	2.17	0.99	1
TL	TL240	236.54	0.036	−0.037	2.40	2333.81	2.40	0.99	3
σ	1.16	0.0001	0.0006	0.89	1378.92	0.89	0.0003		
CL	CL30	30.54	0.09	–	2.76	1152.64	2.76	0.95	3
σ	1.49	0.003	–	0.19	68.07	0.19	0.05		
CL	CL40	40.50	0.094	–	3.16	2202.62	3.16	0.97	4
σ	1.70	0.01	–	0.48	605.71	0.48	0.04		
CL	CL80	75.10	0.068	–	3.31	2378.84	3.31	0.97	4
σ	1.49	0.003	–	0.94	446.12	0.94	0.04		
CL	CL200	194.94	0.055	–	3.18	3208.09	3.18	0.95	5
σ	16.79	0.002	–	0.84	866.99	0.84	0.05		

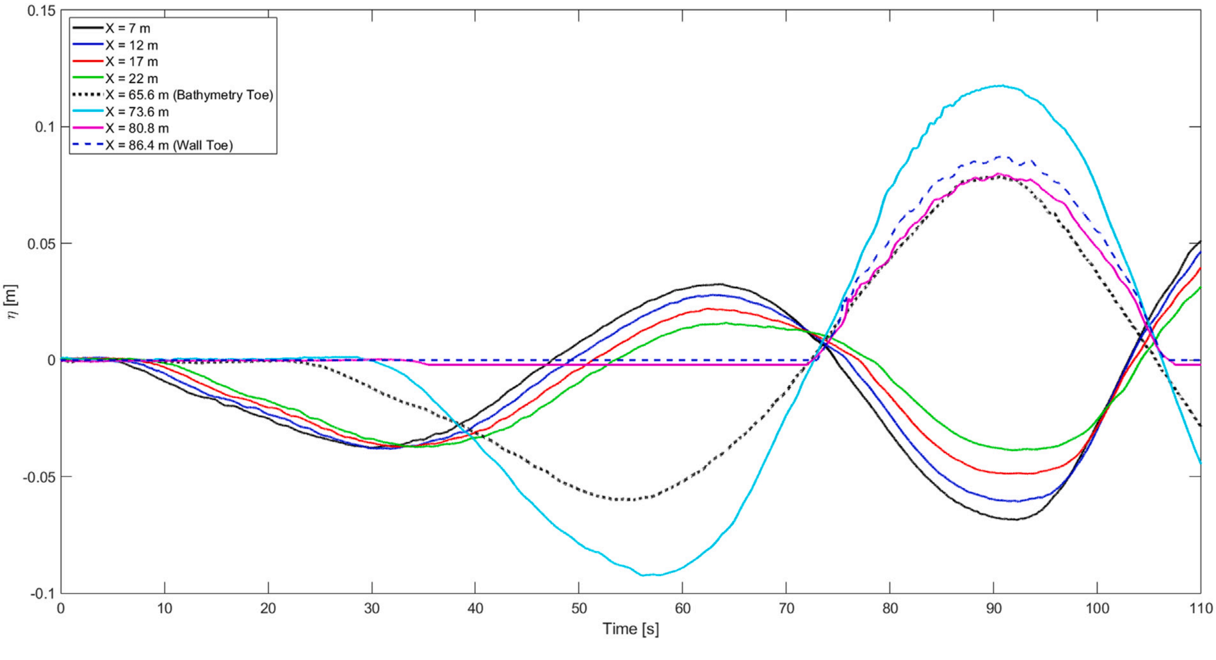

Fig. A.1. The propagation down the flume of a TL80 s wave. The location of the bathymetry toe, where the wave is defined and the wall wave gauges are shown.

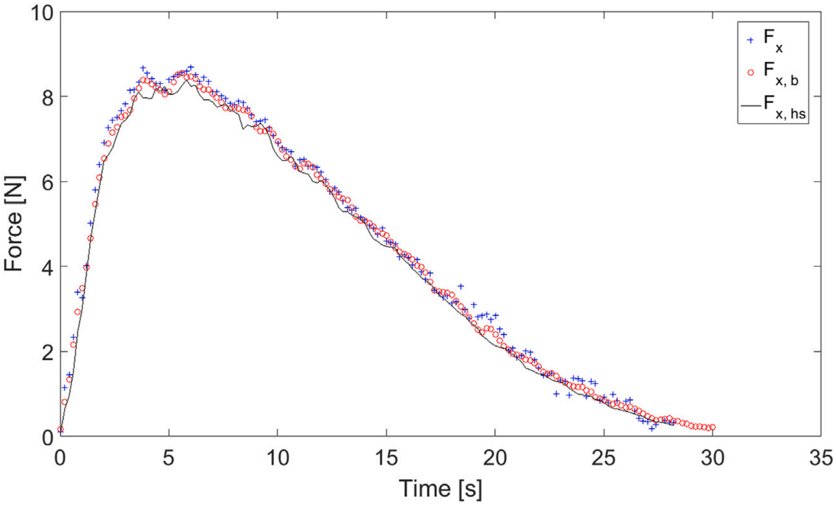

Fig. C.2. Comparison of $F_{x,b}(t)$ estimated from the load cell, $F_x(t)$ from the integration of the pressure transducers and $F_h(t)$ from Eq. (6). For this particular wave (trough-led, $T \approx 53$ s) the forces recorded are hydrostatic.

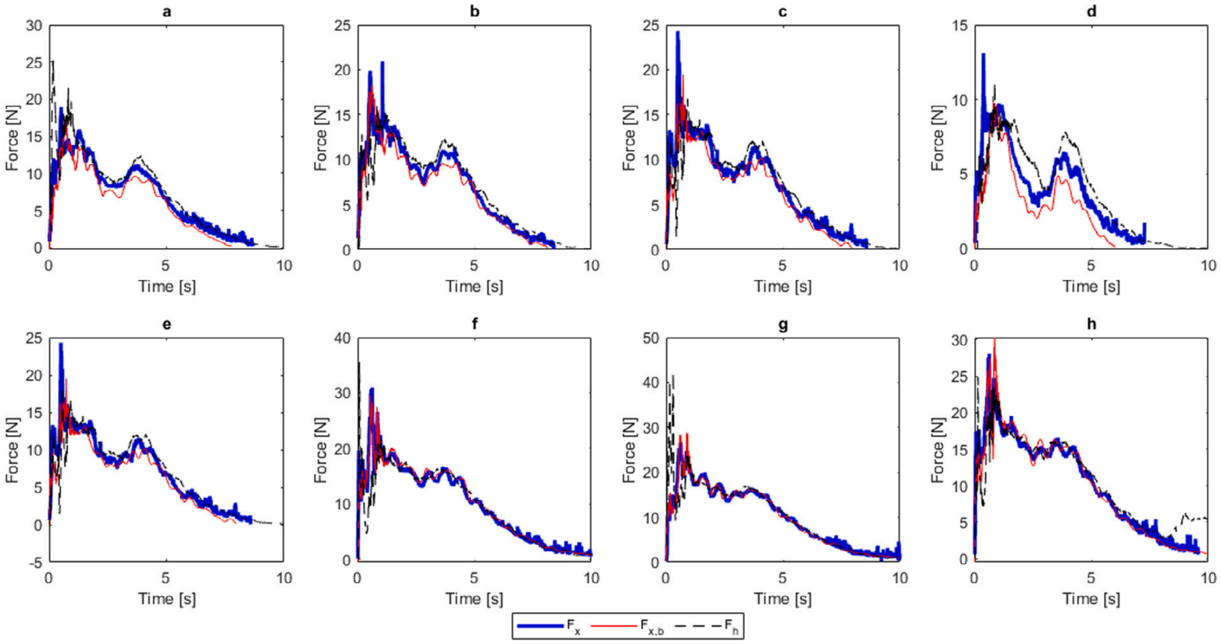

Fig. C.3. Comparison of the recorded time series loading of the h_{wall} = 0.25 m of $F_{x,b}(t)$, $F_x(t)$ and $F_h(t)$ of 8 repeated trough-led, $T \approx 23.5$ s waves that broke greater than 1 m from the h_{wall} = 0.25 m wall.

Appendix B. Instrument calibration

The calibration details and methods for the instrumentation used are as follows. For the resistance type wave gauges, these are calibrated in known incremental depths of water to give a voltage as a function of water depth. A linear regression of the voltages is made to provide calibration gradients, of which an R^2 of 0.9999 or better is demanded. The calibration gradient is recorded and compared throughout the experimental campaign to confirm consistency in the calibration fits and R^2 values across all calibrations.

For the load cell, the calibration is performed in-situ to define the linear response coefficients for each force vector. $F_{x,b}$ response is calibrated using a weighted pulley system attached to the walls vertical surface. $F_{x,b}$ is measured as voltages to which a linear regression is applied to give a calibration to convert to Newtons. The calibration is performed in-situ for each force vector by pulling the structure in the corresponding direction to the vector being calibrated using a weighted pulley system.

The pressure transducers are calibrated by immersion in water at incremental heights to give linear coefficients of voltage to h. The total pressure recorded by the transducers is estimated from Eq. (12) which extends the pressure to the estimated full height h of the water by a linear fit at the wall at a particular time t.

$$p_{total} = \int_0^h p(z)dz \tag{12}$$

where $p(z)$ is estimated from the linear interpolation of the recorded pressure at each transducer and dz is the change in height between each $p(z)$ value. F_x is then the product of $p(z)$ with width b of 0.1 m, equal to the width of the cantilevered wall segment.

Appendix C. Error and repeatability

As the load cell operates by monitoring the piezoelectric charge from a crystal under stress, the error from 'charge drift' over time is calculated as the quotient of the electrical drift in the piezoelectric cell of 0.05 pC/min, (where pC = Pico Coulomb) and the sensitivity of 10 pC/N. For the settings used in these tests the charge drift is 0.3 N/min; negligible over the length the longest test duration ($T \approx 240$ s, Table 1).

Fig. C.2 presents the horizontal force experienced by the 25 cm wall for a typical wave inundation (trough-led, $T \approx 53$ s) using the three different methods of load estimation; the load cell $F_{x,b}(t)$, the pressure transducers $F_x(t)$ and $F_h(t)$ from Eq. (6). The three methods show good agreement with slightly higher readings given by the integration of pressure attributable to the integration of a limited number of point measurements. Single transducers do not account for variations in pressure over their representative area. This can be minimised by using an increased spatial distribution of transducers and by comparison with a direct force measurement. The use of pressure transducers has advantages in allowing spatial non-linearity in impulsive inundations to be captured. The close fit in Fig. C.2 of $F_{x,b}(t)$ $F_x(t)$ and $F_h(t)$ show that the loading for this wave is hydrostatic.

For the repeated waves, given in Table 1, the mean (μ) and standard deviation (σ) of the positive a^+ and negative a^- amplitude, celerity C, wavelength λ and the potential energy E_p of each waveform is also given. The values for all these parameters are small and of the same order of magnitude as the error, indicating the experimental set-up is repeatable.

Fig. C.3 shows the recorded time series loading of the $h_{wall} = 0.25$ m of $F_{x,b}(t)$, $F_x(t)$ and $F_h(t)$. This is for a selection of 8 repeated trough-led $T \approx 23.5$ s waves that break greater than 1 m from the wall, to examine the impact of a more developed bore front on the wall. The figure shows that the repeatability of the loading time series between these waves, despite their inherent non-linearity of the bore fronts, is good.

References

Al-Faesly, T., Palermo, D., Nistor, I., Cornett, A., 2012. Experimental modelling of extreme hydrodynamic forces on structural models. Int. J. Prot. Struct. 3 (4).

ASCE, 2022. ASCE/SEI 7-22 chapter 6: Tsunami loads and effects. Tsunami Loads and Effects, ASCE/SEI.

Bredmose, H., Peregrine, D.H., Bullock, G.N., 2009.. Violent breaking wave impacts. Part 2: Modelling the effect of air. J. Fluid Mech. 641, 389–430.

BSI, 2000. British standards BS-6349. Maritime structures Part 1: Code of practice for general criteria. BSI, BSI, London, UK..

CCH, 2000. Regulations within flood hazard districts and developments adjacent to drainage facilities. Honolulu, Hawaii: City and county of Honolulu building code. CCH, City and County of Honolulu.

Chandler, I.D., Allsop, W., Robinson, D., Rossetto, T., 2021. Evolution of pneumatic Tsunami simulators - From concept to proven experimental technique. Front. Built Environ. 7, http://dx.doi.org/10.3389/fbuil.2021.674659.

Chock, G., Robertson, S.E., Kriebel, D., Francis, M., Nistor, I., 2013. Tohoku, Japan, Earthquake and Tsunami of 2011. ASCE.

Cross, R., 1967. Tsunami surge forces. J. Waterw. Harbor Div. 93, 201–231..

Cuomo, G., Allsop, W., Bruce, T., Pearson, J., 2010a. Breaking wave loads at vertical sseawalls and breakwaters. Coast. Eng. 57, 424–439.

Cuomo, G., Allsop, N.W.H., McConnell, K.J., 2003. Dynamic wave loads on coastal structures: Analysis of impulsive and pulsating wave loads. In: Proc. Conf. Coastal Structures 2003. ASCE / COPRI, pp. 356–368.

Cuomo, G., Allsop, N.W.H., Takahashi, S., 2010b. Scaling wave impact pressures on vertical walls. Coast. Eng. 57 (6), 604–609.

d' Angremond, K., van Roode, F.C., 2004. Breakwaters and Closure Dams. Spon Press.

EEFIT, 2011. The Mw9.0 Tohoku Earthquake and Tsunami of 11th March 2011. Report no, Institution of Structural Engineers.

EEFIT, 2013. Recovery Two Years After the 2011 Tohoku Earthquake and Tsunami: A Return Mission Report By EEFIT. Report no, Institution of Structural Engineers.

FEMA, 2000. FEMA Coastal Construction Manual. Publication Number FEMA55. Publication Number FEMA55.

FEMA, 2008. FEMA P646, guidelines for design of structures for vertical evacuation from Tsunamis. FEMA, Federal Emergency Management Agency, Washington, USA.

Foster, A.S.J., Rossetto, T., Allsop, W., 2017. An experimentally validated approach for evaluating Tsunami inundation forces on rectangular buildings. Coast. Eng. (under Review).

Fraser, S., Raby, A., Pomonis, A., Goda, K., Chian, S.C., Macabuag, J., Offord, M., Saito, K., Sammonds, P., 2013. Tsunami damage to coastal defences and buildings in the March 11th 2011 Mw9.0 Great East Japan earthquake and Tsunami. Bull. Earthq. Eng. 11, 205–239.

Goda, Y., 1974. New wave pressure formulae for composite breakwaters. In: Proceedings of the 14th International Conference on Coastal Engineering. ASCE, New York, pp. 1701–1720.

Goda, Y., 1995. Japan's design practice in assessing wave forces on vertical breakwaters. In: Kobayashi, N., Demirbilek, Z. (Eds.), Chapter 6 in Wave Forces on Inclined and Vertical Wall Structures. ASCE, New York, pp. 40–155.

Goda, Y., 2010. Random Seas and Design of Maritime Structures, third ed..

Goda, Y., Tabata, T., Yamamoto, S.t.e., 2002. PHB, technical standards and commentaries for port and harbour facilities in Japan. In: Goda, Y., Tabata, T., Yamamoto, S. (Eds.), 2002 Technical Standards and Commentaries for Port and Harbour Facilities in Japan. the Overseas Coastal Area Development Institute of Japan, Tokyo.

Goda, Y., Tabata, T., Yamamoto, S.t.e., 2014. PHB, Technical Standards and Commentaries for Port and Harbour Facilities in Japan. Report no, The Overseas Coastal Area Development Institute of Japan, Tokyo.

Goseberg, N., Wurpts, A., Schlurmann, T., 2013. Laboratory-scale generation of Tsunami and long waves. J. Coast. Eng. 79, 57–74.

Hiroi, I., 1920. The force and power of waves. Engineer 184–187.

Holthuijsen, L., Booij, N., Ris, R., 1993. A spectral wave model for the coastal zone.. In: Proceedings 2nd International Symposium on Ocean Wave Measurement and Analysis. New Orleans, Louisiana, July 23–28, New York, pp. 630–641.

Hughes, S.A., 1995. Physical Models and Laboratory Techniques in Coastal Engineering. In: Advanced Series on Ocean Engineering, World Scientific Publishing Co.

Kajitani, Y., Chang, S.E., Tatano, H., 2011. Economic impacts of the 2011 Tohoku-Oki earthquake and Tsunami. Earthq. Spectra 29 (S1), 457–478.

Kihara, N., Niida, Y., Daisuke, T., Kaida, H., Shibayama, A., Miyagawa, Y., 2015. Large-scale experiments on Tsunami-induced pressure on a vertical tide wall. Coast. Eng. 99, 46–63.

Lynett, P., Liu, P., Sitanggang, K., Kim, D., 2008. Modeling Wave Generation, Evolution, and Interaction with Depth-Integrated, Dispersive Wave Equations. COULWAVE Code Manual. Cornell University Long and Intermediate Wave Modeling Package 2.0, 1–90.

Ma, G., Shi, F., Kirby, J.T., 2012. Shock-capturing non-hydrostatic model for fully dispersive surface wave processes. Ocean Model. 43–44, 22–35.

McGovern, D.J., Robinson, T., Chandler, I.D., Allsop, W., Rossetto, T., 2018. Pneumatic long-wave simulation of Tsunami-length waveforms and their runup. Coast. Eng. 138, 80–97.

McGovern, D.J., Todd, D., Rossetto, T., Whitehouse, R.J.S., Monaghan, J., Gomes, E., 2019. Experimental observations of Tsunami induced scour at onshore structures. Coast. Eng. 152.

Mori, N., Takahashi, T., 2012. The 2011 Tohoku earthquake and Tsunami joint survey group. Nationwide post event survey and analysis of the 2011 Tohoku earthquake and Tsunami. Coast. Eng. J. 54, 1–27.

Nandasena, N.A.K., Sasaki, Y., Tanaka, N., 2012. Modeling field observations of the 2011 Great East Japan Tsunami: Efficacy of artificial and natural structures on Tsunami. Coast. Eng. 67, 1–13.

NILIM, 2013. A draft manual for developing earthquake-tsunami disaster scenarios including damage to public works. NILIM.

Nouri, Y., Nistor, I., Palermo, D., Cornett, A., 2010. Experimental investigation of Tsunami impact on free standing structures. Coast. Eng. 52 (10), 43–70.

Palermo, D., Nistor, I., Al-Faesly, T., Cornett, A., 2013. Impact of Tsunami forces on structures. Int. J. Tsunami Soc. 32 (2), 58–76..

Palermo, D., Nistor, I., Nouri, Y., Cornett, A., 2009. Tsunami loading of near-shoreline structures: A primer. Can. J. Civil Eng. 36 (11), 1804–1815.

Peakall, J., Warburton, J., 1996. Surface tension in small hydraulic river models-the significance of the Weber number. J. Hydrol. 53, 199–212.

Raby, A., Macabuag, J., Pomonisc, A., Wilkinson, S., Rossetto, T., 2015. Implications of the 2011 Great East Japan Tsunami on sea defence design. Int. J. Disaster Risk Reduct. 14, 332–346.

Ramsden, J.D., 1996. Forces on a vertical wall due to long waves, bores, and dry-bed surges. J. Waterw. Port Coast. Ocean Eng. 122 (3), 134–141.

Ramsden, J.D., Raichlen, F., 1990. Forces on vertical wall caused by incident bores. J. Waterw. Port Coast. Ocean Eng. 116, 592–613.

Robertson, I.N., Paczkowski, K., Riggs, H.R., Mohamed, A., 2013. Experimental investigation of Tsunami bore forces on vertical walls. J. Offshore Mech. Arct. Eng. 135.

Rossetto, T., Allsop, W., Charvet, I., Robinson, D., 2011. Physical modelling of Tsunami using a new pneumatic wave generator. J. Coast. Eng. 58, 517–527.

Sainflou, G., 1928. Essai sur les digues maritimes verticales: Annales des ponts et Chaussees. Partie Technique 98 (IV), 5–48.

Schimmels, S., Sriram, V., Didenkulova, I., 2016. Tsunami generation in a large scale experimental facility. J. Coast. Eng. 110, 32–41.

Shafiei, S., Melville, B.W., Shamseldin, A.Y., 2016. Experimental investigation of Tsunami bore impact force and pressure on a square prism. Coast. Eng. 110, 1–16.

Shibayama, T., Esteban, M., Nistor, H., Danh Thao, N., Matsumaru, R., Mikami, T., Aranguiz, R., Jayaratne, R., Ohira, K., 2013. Classification of Tsunami and evacuation areas. Nat. Hazards 67, 365–386.

Sriram, V., Didenkulova, I., Sergeeva, A., Schimmels, S., 2016. Tsunami evolution and run-up in a large scale experimental facility. J. Coast. Eng. 111, 1–12.

Takabatake, D., Kihara, N., 2014. Revisit the Tsunami hydrodynamic force on the front of onshore structures. In: Proceedings of the International Coastal Engineering Conference. ICCE2014, ASCE.

Tanimoto, K., Takayama, T., Murakami, K., Murata, S., Tsuruya, H., Takahashi, S., Morikawa, M., Yoshimoto, Y., Nakano, S., Hiraishi, T., 1983. Report no, Ministry for Transport: Japan.

Thomas, R.S., Hall, B., 1992. Seawall Design. Butterworth – Heinemann, Oxford.

Tomiczek, T., Prasetyo, A., Mori, N., Yasuda, T., Kennedy, A., 2016. Physical modelling of Tsunami onshore propagation, peak pressures, and shielding effects in an urban building array. Coast. Eng. 117, 97–112.

US Army Corps of Engineers, U., 1984. Shore Protection Manual, fourth ed. U.S. Govt. Printing Office, Washington D.C..

US Army Corps of Engineers, U., 2006. Coastal Engineering Manual. EM 1110-2-1100, publn. by Coastal & Hydraulics Laboratory, URL http://chl.erdc.usace.army.mil/cem.

Van der Meer, J.W., Allsop, N.W.H., Bruce, T., De Rouck, J., Kortenhaus, A., Pullen, T., Schüttrumpf, H., Troch, P., Zanuttigh, B., 2018. Manual on wave overtopping of sea defences and related structures. EurOtop, Available from: URL https://www.overtopping-manual.com.

Yeh, H., 2006. Maximum fluid forces in the runup zone. J. Waterw Port Coast. Ocean Eng. 132 (6), 496–500.